FIBER OPTIC QUENCH DETECTION VIA OPTIMIZED RAYLEIGH SCATTERING IN HIGH-FIELD YBCO ACCELERATOR MAGNETS

Final Report for STTR Project Starting 6/17/2011, ending 8/7/2015

Small Business: Muons, Inc.
552 N. Batavia Ave.
Batavia, IL 60510

Muons, Inc. PI: Dr. Gene Flanagan

Research Institution: North Carolina State University, Sponsored Project Agreement 2013-0134
Raleigh, NC 27695-7907

Research Inst. PI: Prof. Justin Schwartz

Approved for public release; further dissemination unlimited. (Unclassified Unlimited)

PREPARED FOR THE UNITED STATES

DEPARTMENT OF ENERGY

Work Performed Under grant DE-SC0006251

DISCLAIMER

This report was prepared as an account of work sponsored by an agency of the United States Government. Neither the United States Government nor any agency thereof, nor any of their employees, nor any of their contractors, subcontractors or their employees, makes any warranty, express or implied, or assumes any legal liability or responsibility for the accuracy, completeness, or any third party's use or the results of such use of any information, apparatus, product, or process disclosed, or represents that its use would not infringe privately owned rights. Reference herein to any specific commercial product, process, or service by trade name, trademark, manufacturer, or otherwise, does not necessarily constitute or imply its endorsement, recommendation, or favoring by the United States Government or any agency thereof or its contractors or subcontractors. The views and opinions of authors expressed herein do not necessarily state or reflect those of the United States Government or any agency thereof.

SBIR/STTR RIGHTS NOTICE

These SBIR/STTR data are furnished with SBIR/STTR rights under US DOE Grant No DE-SC0005589 and NCSU Sponsored Project Agreement No. 2010-0054. For a period of four (4) years after acceptance of all items to be delivered under this grant, the Government agrees to use these data for Government purposes only, and they shall not be disclosed outside the Government (including disclosure for procurement purposes) during such period without permission of the grantee, except that, subject to the foregoing use and disclosure prohibitions, such data may be disclosed for use by support contractors. After the aforesaid four-year period, the Government has a royalty-free license to use and to authorize others to use on its behalf, these data for Government purposes, but is relieved of all disclosure prohibitions and assumes no liability for unauthorized use of these data by third parties. This Notice shall be affixed to any reproductions of these data in whole or in part. (End of Notice)

ABSTRACT

Yttrium barium copper oxide (YBCO) coated conductors are known for their ability to operate in the superconducting state at relatively high temperatures, even above the boiling point of liquid nitrogen (77 K). When these same conductors are operated at lower temperatures, they are able to operate in much higher magnetic fields than traditional superconductors like NiTi or Nb3Sn. Thus, YBCO superconducting magnets are one of the primary options for generating the high magnetic fields needed for future high energy physics devices. Due to slow quench propagation, quench detection remains one of the primary limitations to YBCO magnets. Fiber optic sensing, based upon Rayleigh scattering, has the potential for spatial resolution approaching the wavelength of light, or very fast temporal resolution at low spatial resolution, and a continuum of combinations in between. This project has studied, theoretically and experimentally, YBCO magnets and Rayleigh scattering quench detection systems to demonstrate feasibility of the systems for YBCO quench protection systems. Under this grant an experimentally validated 3D quench propagation model was used to accurately define the acceptable range of spatial and temporal resolutions for effective quench detection in YBCO magnets and to evaluate present-day and potentially improved YBCO conductors. The data volume and speed requirements for quench detection via Rayleigh scattering required the development of a high performance fiber optic based quench detection/data acquisition system and its integration with an existing voltage tap/thermo-couple based system. In this project, optical fibers are tightly co-wound into YBCO magnet coils, with the fiber on top of the conductor as turn-to-turn insulation. Local changes in the temperature or strain of the conductor are sensed by the optical fiber, which is in close thermal and mechanical contact with the conductor. Intrinsic imperfections in the fiber reflect Rayleigh backscattered laser signals that are shifted by the changes in the fiber that are induced by a local change in the YBCO temperature or strain. One goal of this project was to show that modern technology can be used to interrogate the signals from a (very expensive) YBCO magnet to detect an impending quench in time to protect it from self-destruction. The results show that Rayleigh-backscattering interrogated optical fibers (RIOF) have significant advantages over traditional techniques, including very high spatial resolution and the ability to detect a hot-spot well before the peak local temperature becomes so high that the conductor can be damaged. RIOF quench detection is intrinsically faster than voltage taps, and this intrinsic advantage is greater as the coil size and/or current margin increases. We describe the development and testing program performed under the grant.

Table of Contents

Project Summary 4

Major Accomplishments of DE-SC0006251 5

Modeling & Parameter Specifications 5

I. Introduction 5

II. Quench detection using a distributed temperature sensor 7

III. Estimating data acquisition and processing time 12

IV. Spatial and temporal resolution trade-offs 14

IV.A. The method 15

IV.B. An example 17

V. A Conceptual Quench Detection Algorithm Based on a DTS 18

VI. Discussion 19

VI.A. Non Steady State Operation Issues 19

VI.B. Selection of optimal resolutions 20

VII. Conclusion 21

Technology Benchmarking 21

Quench Detection System Details 27

System Testing and Coil Results 27

Experimental Details 27

Results & Discussion 29

Bibliography and References 33

Project Summary

Yttrium barium copper oxide (YBCO) coated conductors are known for their ability to operate in the superconducting state at relatively high temperatures, even above the boiling point of liquid nitrogen (77 K). When these same conductors are operated at lower temperatures, they are able to operate in much higher magnetic fields than traditional superconductors like NiTi or Nb3Sn. Thus, YBCO superconducting magnets are one of the primary options for generating the high magnetic fields needed for future high energy physics devices. Due to slow quench propagation, quench detection remains one of the primary limitations to YBCO magnets. Fiber optic sensing, based upon Rayleigh scattering, has the potential for spatial resolution approaching the wavelength of light, or very fast temporal resolution at low spatial resolution, and a continuum of combinations in between. This project has studied, theoretically and experimentally, YBCO magnets and Rayleigh scattering quench detection systems to demonstrate feasibility of the systems for YBCO quench protection systems. Under this grant an experimentally validated 3D quench propagation model was used to accurately define the acceptable range of spatial and temporal resolutions for effective quench detection in YBCO magnets and to evaluate present-day and potentially improved YBCO conductors. The data volume and speed requirements for quench detection via Rayleigh scattering required the development of a high performance fiber optic based quench detection/data acquisition system and its integration with an existing voltage tap/thermo-couple based system. In this project, optical fibers are tightly co-wound into YBCO magnet coils, with the fiber on top of the conductor as turn-to-turn insulation. Local changes in the temperature or strain of the conductor are sensed by the optical fiber, which is in close thermal and mechanical contact with the conductor. Intrinsic imperfections in the fiber that reflect laser signals by Rayleigh scattering are distorted by the changes in the fiber that are induced by a local change in the YBCO temperature or strain. One goal of this project was to show that modern technology can be used to interrogate the signals from a (very expensive) YBCO magnet to detect an impending quench in time to protect it from self-destruction. The results show that Rayleigh-backscattering interrogated optical fibers (RIOF) have significant advantages over traditional techniques, including very high spatial resolution and the ability to detect a hot-spot well before the peak local temperature exceeds the current sharing temperature. Thus, RIOF quench detection is intrinsically faster than voltage taps, and this intrinsic advantage is greater as the coil size and/or current margin increases. We describe the development and testing program performed under the grant.

Major Accomplishments of DE-SC0006251

The major accomplishments of DE-SC000651 have been presented at conferences (including IPAC 2010 (poster), IPAC 2012 (poster), ASC 2012 (poster), ASC 2014 (talk)), industrial meetings (National Instruments Week 2011, National Instruments Week 2014). Much of the work presented at conferences is contained with additional details in the following papers:

Evaluation and implementation of high performance real-time signal processing for Rayleigh scattering based quench detection for high field superconducting magnets. Flanagan, G., Johnson, R. P., Wenzel, L., Schmidt, D., Ruan, Q., Wimmer, C., Chan, W. K. & Schwartz, J. 2012 *IPAC 2012 - International Particle Accelerator Conference 2012.* p. 3602-3604 3 p.

Spatial and temporal resolution requirements for quench detection in (RE)$Ba_2Cu_3O_x$ magnets using Rayleigh-scattering- based fiber optic distributed sensing, Chan, W. K., Flanagan, G. & Schwartz, J. Oct 2013 In : Superconductor Science and Technology. 26, 10, 105015

Quench detection for high temperature superconductor magnets: a novel technique based on Rayleigh-backscattering interrogated optical fibers (RIOF), Scurti, Federico; Ishmael, Sasha; Flanagan, Gene; Schwartz, Justin. Accepted for publication 6/1/2016 Article reference: SUST-101400.R1

In the remainder of the document we describe the work and successes performed as part of DE-SC0006251.

Modeling & Parameter Specifications

I. Introduction

Superconducting magnets based upon high temperature superconductors (HTS) such as $Bi_2Sr_2CaCu_2O_x$ (Bi2212) wires and $YB_2C_3O_y$ (YBCO) coated conductors have very slow quench propagation, as much as two orders-of-magnitude slower than low temperature superconductor-based magnets. As a result, large HTS magnet systems face significant quench detection and protection challenges that must be addressed before reliable, safe operation is realized. Conventional quench detection methods for superconducting magnets continuously monitor resistive voltages on voltage taps sparsely distributed within a magnet, often at the ends of subsections. When the detection system identifies the occurrence of a predetermined quench criterion that signals the onset of a quench, it activates a quench protection event to discharge the magnet and dump the stored magnetic energy into an external device such as a dump resistor. This type of point-probe based detection method, which is very effective for NbTi and Nb_3Sn magnets, only observes the length-averaged behavior of the coil.

Although quench detection systems typically monitor voltage, it is the local temperature profile that dictates the behavior of a quench and the safe operational limits. For HTS systems, slow quench propagation can result in large local temperatures for the same monitored voltage (relative to LTS systems), rendering voltage-based systems ineffective. Furthermore, other limitations to voltage-based quench detection include: (1) the quench-induced resistive voltage

(on the order of few millivolts) needs to be filtered from inductive voltages, during charging or in AC systems, and background noise due to electromagnetic interference, (2) complicated quench detection algorithms monitoring overly pessimistic quench criteria, normally a voltage threshold, are needed to prevent false positives, thus reducing the protection time budget, (3) the location and character of the quench initiation are not obtained with sufficient precision.

An alternative to discretized voltage measurements is distributed temperature sensing (DTS). Ideally, a DTS system allows a quench detection algorithm to extract continuously all necessary temperature related information at any location within a coil with very high spatial and temporal resolution. This would allow the quench detection algorithm to use precise criteria to detect the onset of a quench accurately and quickly while avoiding false-positives that result in unnecessary magnet shut-downs. To date, no DTS system has been installed in a large superconducting magnet, however a DTS system based on a fiber optic sensor (FOS) has the potential to avoid many of the problems and limitations associated with voltage-based quench detection. Moreover, due to their compact size (optical fibers are as small as 50 μm in diameter) and extremely low loss, FOS can potentially be co-wound with very long conductors.

The potential use of a FOS to monitor the strain state and the onset of quenches in Nb_3Sn magnets has been studied intermittently for about 20 years. Mach-Zender interferometry was used to sense a change in the optical path length of the fiber with respect to a reference fiber. More recently, a FOS based on fiber Bragg gratings (FBGs) and Rayleigh backscattering has been considered for HTS magnets; both approaches have been studied with YBCO coated conductor and Bi2212 systems. It was shown that, although the FBG approach can be an effective sensor, it is intrinsically limited to making measurements at predetermined locations and thus suffers from limited spatial resolution due to the a low spatial sampling rate. Rayleigh scattering, however, has been shown to allow measurements nearly continuously along a length of fiber (and thus wire) with spatial resolution that is ultimately limited only by the wavelength of the interrogating light source. While this is a theoretical limit, it is indicative of the potential of the Rayleigh approach. This advantage also proved to be a key challenge to Rayleigh scattering FOS, however, as there is a trade-off between temporal and spatial resolutions in the practical utilization of Rayleigh-based systems due to the large volume of data that is generated and which must be interpreted in real-time.

Rayleigh backscatter in an optical fiber is caused by random fluctuations of the refractive index along the length of the fiber. The fluctuations cause a random, but static scattering amplitude and phase pattern as a function of the fiber length. The fiber can be thought of as having a continuous Bragg grating with random period. Changes in the local period by stimulus such as temperature or strain cause changes in the local reflected spectrum, thus allowing one to calibrate those changes and create a strain/temperature measurement system.

In a Rayleigh-based FOS, swept wavelength interferometry (SWI) measures the reflection coefficient of the sensing fiber. The amplitude of the Rayleigh scattering signal as a function of location is obtained from the Fourier transform of the reflection coefficient. Changes in the fiber condition (e.g. temperature or strain) are sensed in real time by comparing a baseline Rayleigh scattering profile to subsequent scanned profiles. The comparison is performed over a designated number of segments of length Δx, where the number of segments determines the spatial resolution and the number of data points per segment (p) determines the spectral resolution; the more data points per segment, the higher the spectral resolution. Each segment is one sensing element, and thus the spatial and spectral resolutions can be varied. To quantify a local

temperature change (i.e., the change in a segment), the segment data is transformed back to the frequency domain and a cross correlation is performed between the baseline and the new profile for each segment. Any change in a segment manifests as a shift in the correlation peak. The implication for data processing is that if there are N segments and K initial data points (covering the entire fiber under test of length L) then there will be K-point Fourier transforms followed by (N x p-point) cross correlations to be performed. Note that $\Delta x = L/N$ and $p = K/N$.

As a result, Rayleigh scattering for superconducting magnet quench detection is computationally intensive. The computational demands are driven by the volume of signal processing that is required to convert the scattering signature into a temperature signature. The higher the spatial resolution the larger the data volume and thus the lower the temporal resolution with which a data acquisition and processing (DAQ) system can scan the fiber. Therefore, the design of an effective quench detection system based on Rayleigh backscattering FOS must identify the spatial and temporal resolutions that correspond to the safe operation of the magnet; these resolutions can only be determined by careful analysis of the quench behavior of the conductor and magnet.

In this paper, an approach to designing a Rayleigh scattering FOS-based quench detection system for YBCO coated conductor-based magnets is presented. This paper approaches the design from the conductor safety point of view and makes minimal assumptions or tradeoffs based on available computing technologies that would be used to implement the system. The case study of a DAQ system implemented from commercially available products will be discussed elsewhere. The approach first identifies the temporal and spatial resolutions required for effective detection, which is a trade-off driven by the need to detect the onset of a quench with sufficient time remaining to initiate protection before the conductor is damaged. Secondly, the approach parameterizes the capabilities of the quench detection system and the spatial/temporal resolution trade-off for a Rayleigh FOS system. The overlap of the two trade-offs then determines the effective operating space for a Rayleigh FOS system. The approach is then demonstrated with an example and a conceptual quench detection algorithm is presented.

II. Quench detection using a distributed temperature sensor

Distributed temperature sensor requirements

A DTS quench detection system requires active fiber state monitoring and an understanding of strain/temperature profiles associated with normal operation (non-quench). To aid in the rejection of false positives it is also useful to understand the expected strain/temperature profiles associated with a quench. To assist in the development of quench detection and protection for YBCO coils, an experimentally validated, three-dimensional multiscale YBCO conductor and coil models have been developed (W. K. Chan and J. Schwartz, "A hierarchical, three-dimensional, multiscale electro-magneto-thermal model of quenching in REBa2Cu3O7-d coated conductor based coils," IEEE Transactions on Applied Superconductivity, vol. 22, p. 4706010, 2012). The coil model was validated with data from a YBCO pancake coil that was constructed and tested specifically to understand YBCO quench behavior. The coil was comprised of 97 turns of YBCO coated conductor in a single pancake configuration; further details on this coil and the test results were reported elsewhere (H. Song, K. Gagnon, and J. Schwartz, "Quench behavior of conduction-cooled YBa2Cu3O7−δ coated-conductor pancake coils stabilized with brass and copper," Superconductor Science & Technology, vol. 23, p. 10, 2010.). This coil serves as the example throughout this paper because of the existence of both experimental results

and the validated model. The resulting methodology, however, is generally applicable to superconducting coils using a DTS for quench protection.

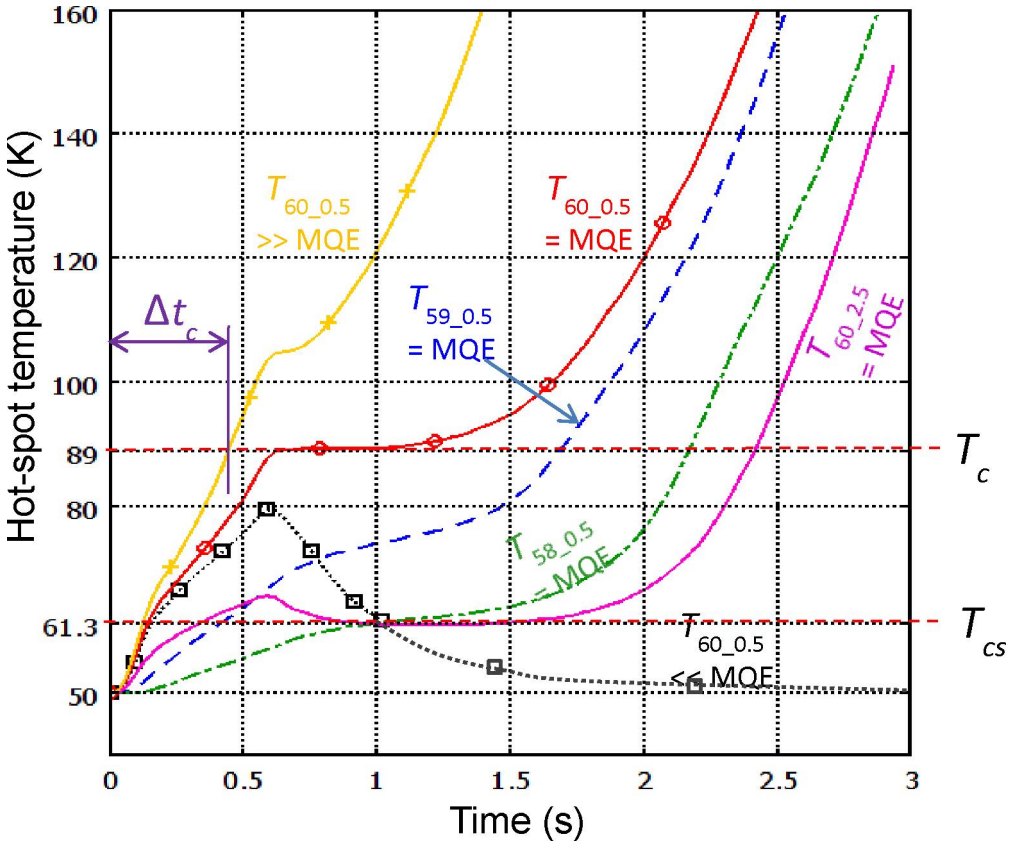

Figure 1. Temperature profiles showing different quench patterns produced by heat disturbances of varying energy at different locations as a function of time in a coil. The profiles are taken from an experimentally validated model of a small pancake coil model consisting of 97 turns. $T_{60_0.5}$ denotes the temperature measured at turn #60 at 0.5 cm away from the center of the heater. Three sets of profiles, corresponding to three different heat energy inputs (QE >> MQE, QE = MQE and QE << MQE), are shown.

Simulation results in Figure 1 indicate that temperature, T, and its gradients, are greatly affected by the details of the heat disturbance configuration (magnitude, length and duration) and the locations of observation relative to the initial hot spot. For example, identifying a lower bound for Δt_c, the time delay before T surpasses the critical temperature, T_c, or an upper bound for dT/dt, the rate at which T increases, at $T = T_c$, is difficult. The time slopes become arbitrarily small and steep, respectively, with arbitrarily large disturbance energy, although they must be bounded because of a finite heat transfer rate. Even if the bounds are found, their lower-upper bound variation ranges are too wide to be useful for drawing conclusive properties to characterize the coil. It is also known that the minimum quench energy (MQE) depends nonlinearly on the heat source length and duration (L. Malinowski, "Analytical method for calculation of critical energy of technical superconductors based on the minimum propagating zone theory," Cryogenics, vol. 30, pp. 765-769, Sep 1990.). Figure 2 illustrates possible quench patterns generated from possible heat disturbances. For a fixed disturbance length and duration, the quench energy (QE) determines the resulting quench pattern. Note that a quench can occur at

any temperature above the current sharing temperature (T_{cs}), and yet a hot-spot with temperature > T_c does not necessarily cause a quench; recovery remains possible. Given that disturbances in coils are unpredictable and can have any configuration, quench detection criteria are based on direct measurement of T, dT/dt or dT/dx become complicated because the quench criteria are not well-defined and the algorithm needs to trace the dynamically changing patterns of the parameters to distinguish a quench from a false positive.

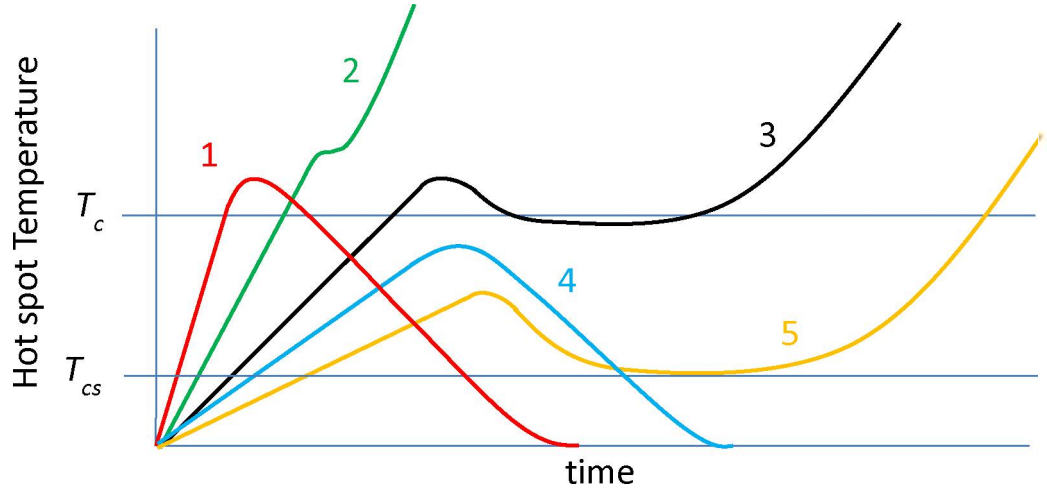

Figure 2. An illustration of possible quench patterns as determined by the heat disturbance configuration. Case 1 is for a large but short-length heat pulse with QE < MQE_1, case 2 is for QE >> MQE_2, case 3 is for QE = MQE_2, and case 4 is for QE << MQE_2. The disturbance durations in cases 2-4 are the same. Case 5 is for a small but long-duration disturbance with QE = MQE_3. The physical lengths of the heat pulses are the same in all cases. Note that the same MQE = MQE_2 is used in cases 2-4, with MQE_1 > MQE_2 > MQE_3. Comparing, for example, case 1 and case 3, if one only bases quench detection on monitoring T(t), then case 1 will likely yield a false positive require very fast detection.

A. Minimum propagating zones as the defining quench characteristic

The minimum propagating zone (MPZ) is a quench parameter (in length) that is independent of the heat disturbance configuration and is only weakly dependent on the temperature profile in the range between T_{cs} and T_c. If the Joule heating energy (less the energy transferred to any cooling), which occurs for $T > T_{cs}$, is larger than a minimum value, a quench occurs. The MPZ is a function of shared current and conductor normal-state electrical conductivity, which in turn are functions of temperature and conductor architecture. The MPZ is therefore determined by T in the range of T_{cs} to T_c only. Extensive simulations show, however, that it is always possible to find a location- and time-independent fixed temperature T_{mpz} which is between T_{cs} and T_c and a fixed (maximum) MPZ (out of a narrow range of MPZs), such that the Joule heating energy created by $J(T_{mpz})$ within a conductor volume of length at least MPZ will initiate a quench, regardless of the heat disturbance configuration. Note that T_{mpz} is only dependent on the conductor properties; it is an intrinsic property. As an example, simulations on the aforementioned pancake coil with T_c = 89 K and T_{cs} = 61.7 K show that when observed at T_{mpz} = 85 K, the MPZs are within a narrow range, from 1.38 cm to 1.54 cm, for any heat disturbance up to 5 cm tested length (1/6 of a turn). The 10% variation is due to the non-uniform distribution of the temperature (and thus J), which is more pronounced for heat disturbances with very long durations. The key point is that the lower- and upper-bound MPZs have a small

difference and occur in cases where the heat disturbance lengths are somewhere between a wide range of tested lengths, ranging from 0.3 cm to 5 cm. This indicates that the MPZ is independent of the heat disturbance length. Given the small variation (0.8 mm half-length) in the MPZs, the fixed MPZ is chosen to be the upper-bound 1.54 cm. The upper-bound MPZ is chosen because it dictates the overall time budgets allowed for detection and protection. The lower-bound MPZ is in general associated with smaller heat disturbances with longer length or duration. In these cases, the temperature rises in a much more gentle way than cases with larger MPZ. As a result, at the time the normal zone has reached the size of the upper-bound MPZ, the peak temperature is about the same as that in the case with the upper-bound MPZ. Therefore, there is no advantage to single-out the lower-bound MPZ; it is safe to use the upper-bound as a unified quench detection criterion.

Another important aspect of using MPZ as a quench detection criterion is that, unlike a temperature profile in case 3 or 5 shown in Figure 2, a MPZ never undergoes an expand-shrink-expand sequence. Once a normal zone is larger than the MPZ, it remains so and a quench occurs. If a normal zone begins to shrink in size before becoming an MPZ, the coil recovers. This fact greatly simplifies quench detection algorithm development and enables decisive, quick discrimination between a quench and a false positive. Furthermore, compare case 1 and case 3. If one only bases quench detection on monitoring T(t), then case 1 will likely yield a false positive. Thus, by using an MPZ-based criterion, the assessment of the temperature data is simplified because the identification of a quench is based solely on the normal zone length; analysis of the detailed temperature profile is not required, and delineation of situations such as case 1 versus case 3 are eliminated.

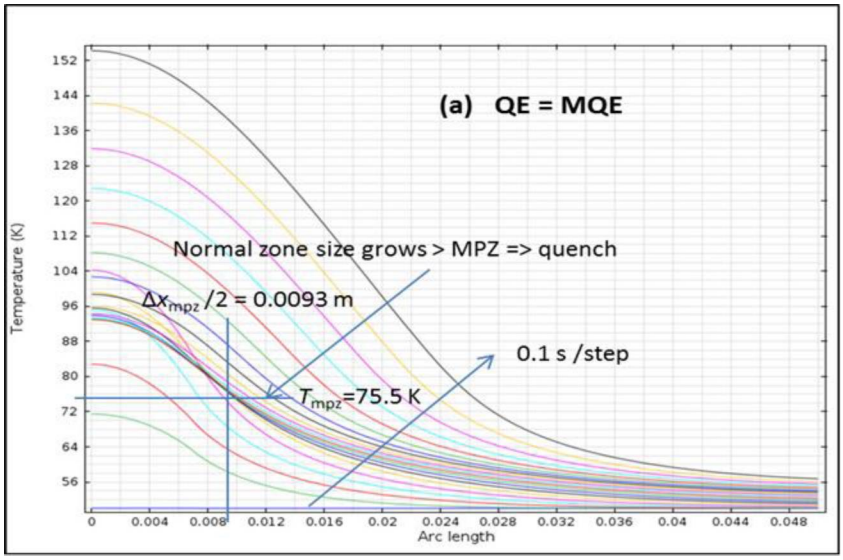

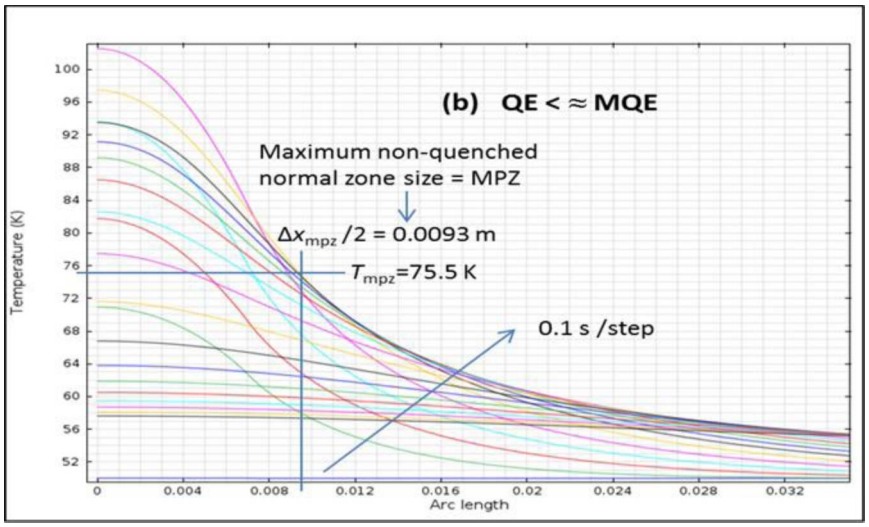

Figure 3. Calculated temperature profiles along the tape length for (a) QE = MQE and (b) QE < MQE. The series of temperature profiles in each figure show the evolution of the temperature in 0.1 s increments. Note that the hot-spot temperature (at $x = 0$) in (a) varies with a pattern similar to case 3 in Figure 2. The hot-spot temperature in (b) varies with a pattern similar to case 1 in Figure 2.

MPZ is a predictable parameter because it is independent of the unpredictable heat disturbance configuration. Thus, it can be used to derive the spatial and temporal resolution requirements for an effective quench detection system based on a distributed sensor. The procedure for finding the MPZ via simulations involves first choosing a series of disturbance configurations (magnitude, length and duration), including one with a large QE magnitude, short length and duration, and one with small QE magnitude, long length and duration. Second, for a particular heat disturbance geometry, the QE is adjusted such that the QE = MQE, as shown in Figure 3(a). Third, the QE is slightly reduced such that QE < MQE, as shown in Figure 3(b). The half-length of the MPZ, $\Delta x_{mpz}/2$, is found as the length (measured from the center of the heat disturbance) of the largest non-quenched normal zone measured at $T = T_{mpz} = 85$ K. This fixed temperature threshold is chosen heuristically by comparing all the simulation results; more study is needed to find a more accurate approach to define the MPZs.

An effective quench detection system is concerned with detecting the quench criteria threshold as soon and as accurately as possible. Thus, the information surrounding the MPZ around the time Δt_{mpz}, which is the time at which a normal zone grows to an MPZ, must be monitored carefully. Referring to Figure 4, besides the MPZ half size, $\Delta x_{mpz}/2$, and onset time Δt_{mpz}, other important parameters for the determination of the spatial and temporal resolutions are the propagation velocity $V_{mpz} = dx_{mpz}/dt$ and the average slope dT_{mpz}/dx; both are observed on the MPZ boundary. Another useful parameter is dT_0/dt, the average rate at which the hot-spot temperature increases at the center of the normal zone, observed at Δt_{mpz}. These parameters are used to derive the requirements for the spatial and temporal resolutions required for quench detection.

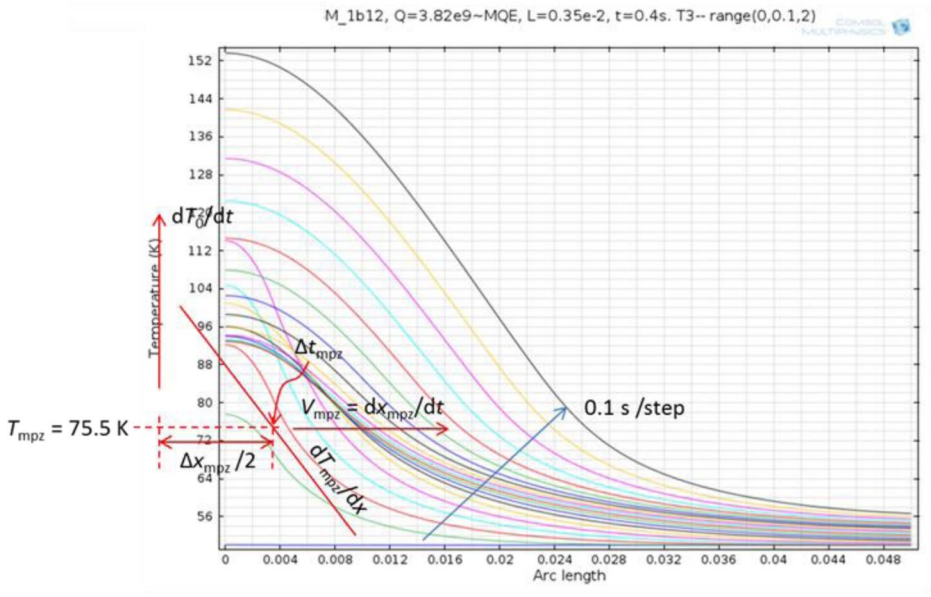

Figure 4. Simulation of quench properties surrounding the MPZ in the coil used in Figure 3.

Simulations from a wide range of heater configurations on the example single pancake YBCO coil model give the following results (with their roles). For other coil configurations, the values will vary with the conductor and coil details, as well as the operating temperature. Nonetheless, they serve as a valuable starting point for further assessment of distributed sensing.

- Δx_{mpz} = 1.38 cm - 1.54 cm, (defines the upper bound for the spatial resolution Δx),
- Δt_{mpz} = 0.015 s - undefined (defines the upper bound for the temporal resolution Δt),
- $V_{mpz} = dx_{mpz}/dt$ = 2.50 cm/s - 14.00 cm/s (defines the relationship between Δx and Δt),
- dT_{mpz}/dx = 7.4 K/cm - 63.0 K/cm (defines sensitivity or accuracy),
- dT_0/dt = 90 K/s - 900 K/s (defines sensitivity or accuracy).

The upper-bound of Δt_{mpz} is undefined because it depends on the duration of the heat source that creates the normal zone. The lower-bounds of V_{mpz}, dT_{mpz}/dx and dT_0/dt are defined, however, because they are observed when the normal zone has grown into an MPZ where the Joule heating (not the heat source) maintains the normal zone propagation while the residual heat from the heat pulse has subsided. It is important to emphasize that regardless of the configuration (in magnitude, length and duration) of the initial source of the normal zone, if the normal zone grows into an MPZ, then for the example in Figure 3 the MPZ is never shorter than 1.38 cm or longer than 1.54 cm. It is also important to note that V_{mpz} is different from normal zone propagation velocity (NZPV) commonly reported in the literature. NZPV measures the propagation velocity caused by the Joule heating when the residual heat from the initial heat source has subsided. Here, V_{mpz} is the propagation velocity when the MPZ is forming, though it may or may not still be under the influence of the initial heat disturbance.

III. Estimating data acquisition and processing time

Before deriving the requirements for the quench detection resolutions, it is necessary to understand the relationship between the general DAQ system's segment length, Δx, and the total time needed to capture and process a Rayleigh backscatter signal (Δt_{daq}) such that a temperature measurement results (see [32] for details). Without specifying any particular data processing technology, Δt_{daq} is estimated in a general computational platform as:

$$\Delta t_{daq} = \left(K\log(K) + Np\log(p)\right)\Delta t_{fft} + (N+1)\Delta t_{lead} + \left((K-1) + N(p-1)\right)\Delta t_{burst} + \Delta t_{daqio} \quad (1)$$

where K is the total number of points, N is the number of segments and $p = K/N$ is the number of fast Fourier transform (FFT) data points per segment. The two log terms are the time required to calculate the FFT and the cross correlation, with Δt_{fft} being the computational time for each single FFT summation. The computation can either be executed on a CPU[1]-based, GPU[2]-based or FPGA[3]-based platform (G. Flanagan, R. P. Johnson, L. Wenzel, D. Schmidt, Q. Ruan, C. Wimmer, W. K. Chan, and J. Schwartz, "Evaluation and Implementation of High Performance Real-Time Signal Processing for Rayleigh Scattering Based Quench Detection for High Field Superconducting Accelerator Magnets," in 2012 International Particle Accelerator Conference, 2012.). A complete data transfer cycle, either between a cache and main memory on a CPU-based system or between GPU/FPGA and CPU (via an I/O interface) on a GPU/FPGA-based system, begins with a leadoff cycle with a long latency, followed by a series of consecutive fast burst transfer cycles. The Δt_{lead} term is the leadoff latency time required to transfer the first unit of data. The Δt_{burst} term is the time required to transfer the remaining data units in burst transfer cycles. The last term, Δt_{daqio}, is the time to capture and transfer the measured data from the data acquisition unit to the data processing system. Here, for simplicity, the effects of the probability of cache misses and I/O bus conflicts (due to different data size) on the data transfer performance are ignored. Each data transfer is assumed to always begin with a lead-off cycle, followed by a series of burst cycles.

Using $N=L/\Delta x$ and $p = K/N = \Delta x K/L$, where L is the length of the fiber section under test, the total processing time Δt_{daq} as a function of segment length Δx becomes

$$\Delta t_{\text{daq}} = K\left(\log(K)+\log\left(\Delta x\frac{K}{L}\right)\right)\Delta t_{\text{fft}} + \left(\frac{L}{\Delta x}+1\right)\Delta t_{\text{lead}} + \left(2K-1-\frac{L}{\Delta x}\right)\Delta t_{\text{burst}} + \Delta t_{\text{daqio}}. \quad (2)$$

Figure 5 gives an example showing Δt_{daq} as a function of Δx using fictitious values mimicking a CPU-based system. Note that when both Δt_{fft} and Δt_{lead} are sufficiently large, as in this example, the leadoff latency dominates for small Δx while the FFT computational time dominates when Δx is large (thus more computational data points in each cross correlation FFT).

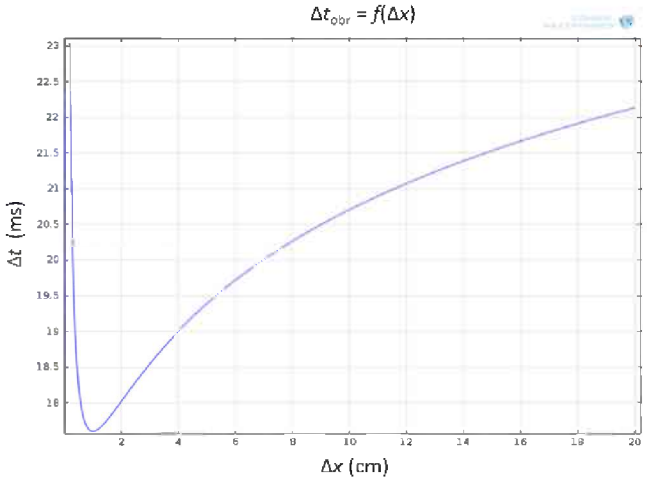

Figure 5. A particular Δt_{daq} function plot with L = 51.2 m, K = 512000 points, $\Delta t_{\text{fft}} = 1 \times 10^{-8}$ s, $\Delta t_{\text{lead}} = 4.5 \times 10^{-7}$ s, $\Delta t_{\text{burst}} = 1 \times 10^{-8}$ s and $\Delta t_{\text{daqio}} = 0$ s.

[1] Central Processing Unit
[2] Graphics Processing Unit
[3] Field Programmable Gate Array

Given the nondeterministic and complicated nature of modern computer architectures, it is not easy to write an equation explicitly for Δt_{fos}, especially one that takes into account the probability of occurrence of each timing component. An alternate way to estimate Δt_{fos} as a function of Δx is to derive statistically the data processing time from a large number of experimental runs with vastly different Δx sizes. This method does not require detailed timing knowledge of the underlying DAQ technology. However, it also gives no insights into the potential performance bottlenecks of the technology. Knowing the bottlenecks of the DAQ technology allows one to refine the Δx sizes and computation algorithms or choose more appropriate hardware components to mitigate the impact on performance.

IV. Spatial and temporal resolution trade-offs

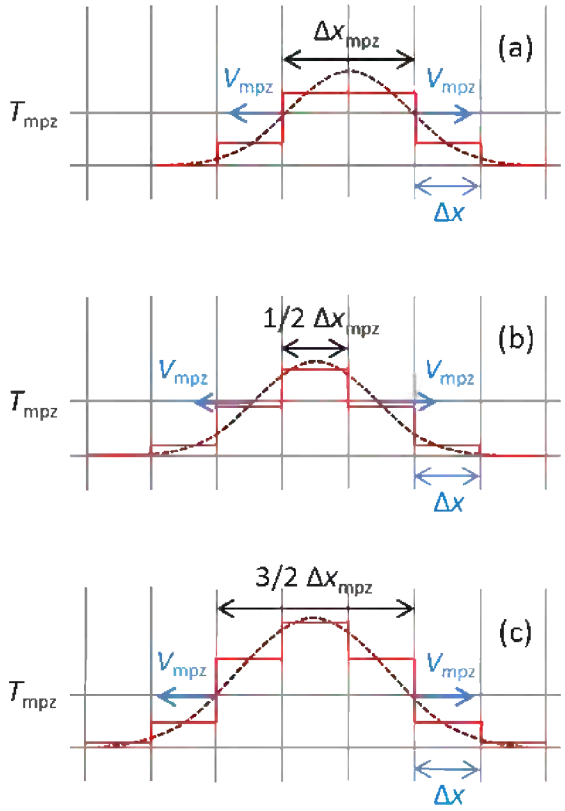

Figure 6. (a) An MPZ temperature profile. The dashed curve is the actual hot spot temperature profile of a MPZ with width = Δx_{mpz} when measured at T_{mpz}. The solid step-wise curve is what is actually seen by a FOS-based quench detection algorithm. The hot spot pulse grows with a speed of V_{mpz}. (b) Worst case scenario; the spatial sampling grid is shifted by $\Delta x_{mpz}/2$, resulting in only 1/2 of the MPZ being seen. As a result, the onset of the MPZ is not detected. (c) After $\Delta t = (\Delta x - \Delta x_{mpz}/2)/V_{mpz}$, the hot spot expands to a size of 3/2 Δx_{mpz}, resulting in 3/2 of the MPZ being seen. As a result, the MPZ is finally detected.

The analysis developed here is based on the MPZ as the key quench detection criterion, and thus the analysis begins with the temperature profile. A typical hot-spot spatial temperature profile (along the tape length), as depicted in Figure 6, looks like a Gaussian function. In practice, the distributed temperature profile translated from a series of cross correlations on segments of Rayleigh scatter spectra along the fiber length contains significant noise. A general guide to deal with noise is to use uniform sampling intervals that are at least four times smaller than the full-width at half-maximum of the measured Gaussian function. The situation in quench detection,

however, is different because the size of the temperature variations as observed by a FOS evolves dynamically. Moreover, the goal in a quench detection system is not to rebuild the temperature profile with high accuracy but to recognize the MPZ (its width measured at a temperature threshold) as quickly as possible. Therefore, sampling theory will not be used but instead a heuristic reasoning approach is applied to determine the basic requirements for finding proper resolutions required for deterministic, fast and reliable quench detection. The actual efficiency of the methods depends on the quality of the FOS measurement and will be evaluated and refined experimentally.

The cross correlation of two spectra tells us the measure of similarity between the two spectra when a time lag is applied to all or part of one of the spectra. An important property of SWI is that a cross correlation on each segment yields a single-peak frequency shift as a measure of similarity, which translates into the sensed temperature in the segment. Thus, the overall distributed temperature profile for the fiber is discretized, as illustrated by the solid line in Figure 6(a). This discretization may cause distortion in the magnitude and length reading of a temperature peak, as illustrated in Figure 6(b), where only half of the MPZ is detected. As a result, the spatial resolution, or equivalently the segment size Δx, must be chosen appropriately to prevent loss of important information. If not handled correctly this could lead to delays in determining if the magnet is quenching or not.

Here, a heuristic approach to find a proper set of resolutions to reliably capture an MPZ before the coil is damaged is discussed. For simplicity the discussion is restricted to the ideal case where the measured distributed temperature profile contains no noise. The need to counter a noisy background during measurement is addressed experimentally. Under a noise-free assumption, two fundamental requirements for choosing proper resolutions are derived. First, a proper spatial resolution, Δx, is required to be $\Delta x <= \Delta x_{mpz}$, where Δx_{mpz} is defined as the upper-bound MPZ. Second, if a normal propagation zone (NPZ) becoming Δx_{mpz} travels at a speed equal to the slowest measured V_{mpz} (measured at $T = T_{mpz}$, see Figure 4) then the temporal resolution Δt is required to be $\Delta t <= \Delta x_{mpz}/V_{mpz}$. In addition, if $(\Delta x-\Delta x_{mpz}/2)/V_{mpz} < \Delta t <= \Delta x_{mpz}/V_{mpz}$ is satisfied, then any Δx and Δt obeying these requirements assures that the MPZ will be identified in the next Δt sampling (if the current sampling fails to capture the onset of the MPZ); see Figure 6 for an illustration. The left hand side in the inequality is the worst-case time required for the NPZ to grow and fill the remaining Δx, which in this case only covers half of the MPZ. Any resolutions not meeting these basic requirements may result in delayed, less predictable MPZ detection.

IV.A. The method

According to the two basic requirements mentioned above, the resolutions, Δx and Δt, are dictated by Δx_{mpz} and V_{mpz}, which are the intrinsic characteristics of a specific conductor and coil. The method discussed below can then be used to identify an appropriate DAQ technology that satisfies the requirements, or to decide if an existing DAQ system matches the coil behavior. Alternatively, if existing DAQ options cannot meet the demands, the conductor or coil design can be altered to improve Δx_{mpz} and/or V_{mpz} to match available DAQ capabilities. Using Figure 7 as an aid, the spatial and temporal resolutions for safe quench detection are identified by:

1. Plot the slowest V_{mpz} (as a function $\Delta t = \Delta x/V_{mpz}$) and $\Delta t_{daq} = f(\Delta x)$ (equation (2)) on a Δt versus Δx coordinate.
2. Form a zone bounded by the upper-bound of Δx_{mpz}, the shortest Δt_{mpz} and the slowest V_{mpz} line as indicated by the dashed-border zone in Figure 7. This zone is intrinsic to the coil and any combination of Δx and Δt within this zone is safe to the coil.

3. Mark Δx_{sen} on the Δx axis. Δx_{sen} is the smallest Δx defined by the lowest signal-to-noise ratio and per-segment sensitivity characterized by the DAQ system.
4. The intersection of Δt_{mpz} and function f at the smallest Δx with $\Delta x > \Delta x_{sen}$, if it exists, gives Δx_{max}. An acceptable spatial resolution Δx must satisfy $\Delta x_{sen} <= \Delta x <= \Delta x_{mpz}$ and Δx_{max} (whichever is smaller).
5. Within the acceptable Δx as outlined in #4 above, the smallest Δt of function f gives Δt_{min}. An acceptable temporal resolution Δt must satisfy $\Delta t_{min} <= \Delta t <= \Delta t_{mpz}$.
6. Confine the dashed-border zone on the Δt axis with Δt_{min} and on the Δx axis with Δx_{sen} and Δx_{max} or Δx_{mpz} (whichever is smaller). This refined zone (represented by the light-grey area in Figure 7) represents the initial admissible zone for the Δx and Δt.
7. An admissible zone contains all the acceptable Δx and Δt such that $\Delta t_{daq} = f(\Delta x) <= \Delta t <= \Delta t_v \equiv \Delta x/V_{mpz}$ and Δt_{mpz}, (whichever is smaller). Here the symbol ≡ means "defined as". Thus, the final admissible zone is where V_{mpz} line is always on top of the f curve. The latter assures that the temporal sampling time is not shorter than the data processing time of the DAQ system. Accordingly, Δx_1 and Δt_{v1} in Figure 7 are acceptable, while Δx_2 and Δt_{v2} are not. The final admissible zone is marked as the dark grey area between the two curves in Figure 7. Steps #4 and #7 together assure that the two fundamental resolution requirements described in the previous section are satisfied
8. If the technology in question has a function f which results in an empty admissible zone, then this technology is not applicable to the given coil. In other words, if the function f of a technology is always greater than the V_{mpz} of a coil for all Δx satisfying $\Delta x_{sen} <= \Delta x <= \Delta x_{mpz}$ and Δx_{max}, then no safe spatial and temporal resolutions are found, and either the conductor or coil must be redesigned, or an alternative detection technology is required.
9. To ensure fast, deterministic capturing of an MPZ, plot $\Delta t = (\Delta x - \Delta x_{mpz}/2)/V_{mpz}$ on the same coordinate to further restrict the admissible zone. The new zone is now represented as the shaded zone in Figure 7. Any Δx and Δt in the shaded region guarantees that a MPZ can be sampled in the next Δt sampling when the current Δt misses the MPZ.

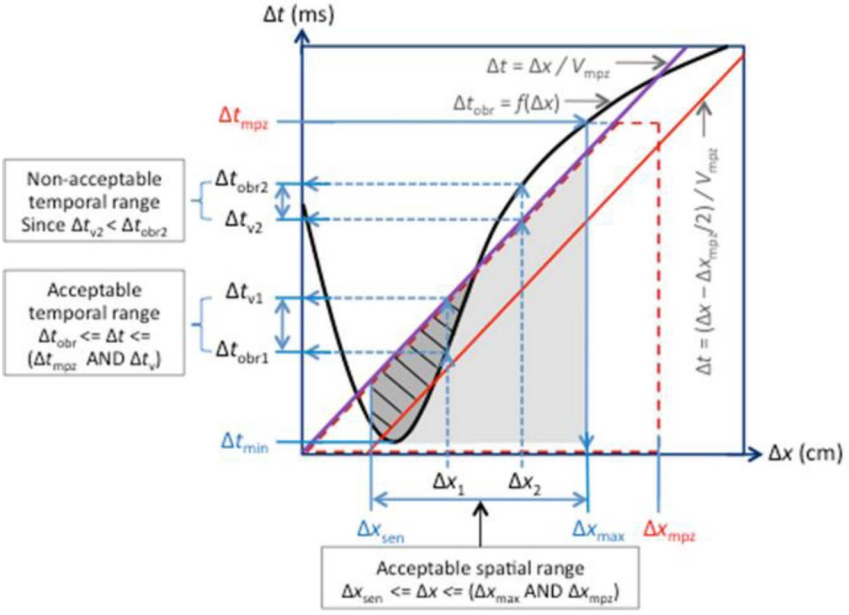

Figure 7. Graphical illustration for the method of determining if a DAQ technology can meet the requirements of a coil in terms of spatial and temporal resolutions and finding the admissible resolutions.

If there is a case that the MPZ's Δx_{mpz} is smaller than the smallest Δx allowed by a DAQ technology, then the technology is not appropriate for the coil. If this technology is the only available solution, then there will be a detection delay of $\Delta t >= (\Delta x - \Delta x_{mpz}) / V_{mpz}$. This can be acceptable if the difference $\Delta x - \Delta x_{mpz}$ is small, V_{mpz} is fast, or the delay plus the detection time is sufficient to protect once a quench is detected.

It is important to note that the procedure stated above only defines an admissible zone for the spatial and temporal resolutions. Other factors, such as the time required to protect, must be factored into the design of the detection system. Once the operating resolutions are selected, the required sensitivity (not the one specified by the DAQ system) is calculated to define a new Δx_{sen}, which is then used to refine the shaded admissible zone. The process of finding the optimal resolutions and the required Δx_{sen} repeats until the condition $\Delta x_{sen} <= \Delta x$ is satisfied. The process of finding Δx_{sen} and optimal resolutions are given in the next and the Discussion sections, respectively.

IV.B. An example

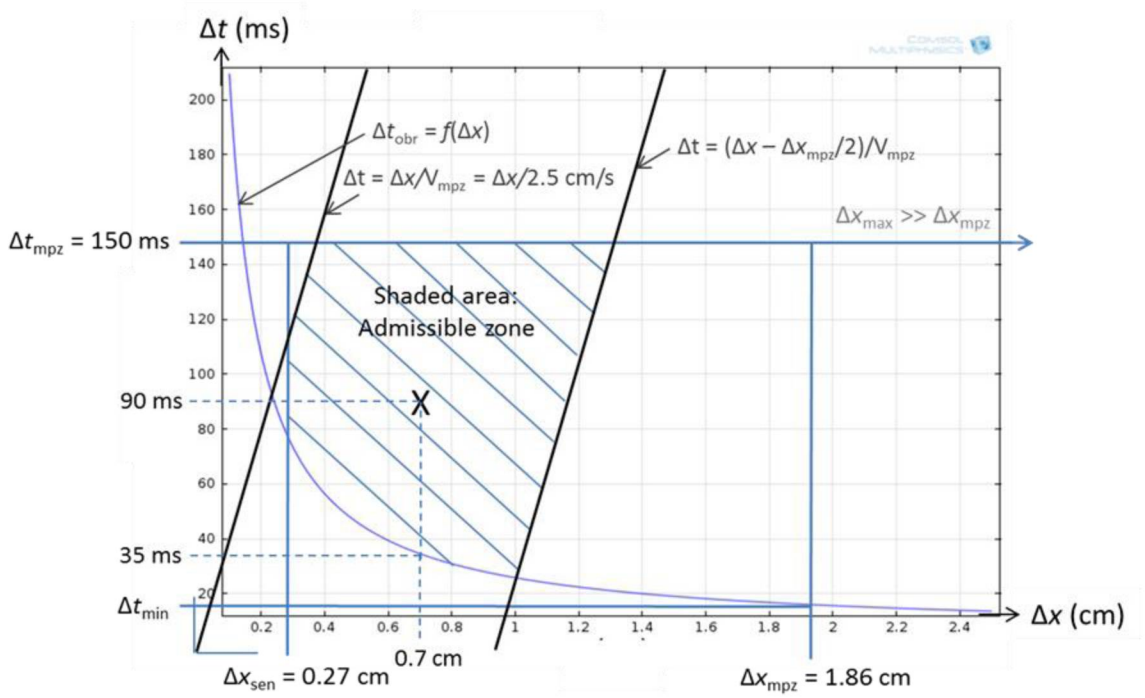

Figure 8. An example showing how to identify admissible spatial and temporal resolutions, and also to find Δx_{sen} and optimal resolutions.

Suppose one intends to apply a DAQ system with a computation function f governed by the following timing parameters to monitor the example pancake coil. The timing parameters are $\Delta t_{fft} = 0.3 \times 10^{-9}$ s, $\Delta t_{lead} = 4 \times 10^{-6}$ s, $\Delta t_{burst} = 1 \times 10^{-8}$ s and $\Delta t_{daqio} = 5 \times 10^{-3}$ s. These timing parameters resemble the timings found in a typical GPU-PCI based data processing system. The function $\Delta t_{daq} = f(\Delta x)$ is plotted in Figure 8. The length of the co-wound fiber L is 51.2 m and the total data points K along L is 512000 points. With $\Delta x_{mpz} = 1.54$ cm, $\Delta t_{mpz} = 0.15$ s, $V_{mpz} = 2.50$

cm/s, dT_{mpz}/dx = 7.4 K/cm and dT_0/dt = 90 K/s, and assuming that the best-case noise-limited spatial resolution Δx_{sen} intrinsic to the DAQ system is found experimentally to be 0.25 cm, then one can follow the steps outlined in the previous section to find that the given DAQ is indeed a suitable technology. Adapting the same steps, the admissible resolutions that guarantee an appropriate detection time are found in the shaded region shown in Figure 8.

Now consider as an example Δx = 0.5 cm and Δt = 60 ms. Using dT_{mpz}/dx and dT_0/dt, one can estimate the minimum spatial resolution Δx_{sen} needed to maintain sufficient accuracy in the temperature measurements:

1. Approximating $\Delta T \approx (dT_{mpz}/dx)\Delta x$, where dT_{mpz}/dx is the least steep slope at the MPZ boundary measured at Δt_{mpz}, one gets ΔT = 7.4 K/cm x 0.5 cm = 3.7 K. This requires that the per-segment temperature sensitivity or accuracy must be at least ΔT.
2. Approximating $\Delta T \approx (dT_0/dt)\Delta t$, where dT_0/dt is the slowest temperature increasing rate at the center of the hot spot when the MPZ is reached, one gets ΔT = 90 K/s x 60 ms = 5.4 K per time step. This also requires that for any chosen segment size Δx, the per-segment temperature sensitivity should be at least 5.4 K.

From these data, the temperature sensitivity is required to be at least 3.7 K per segment, and the smallest segment size defined as Δx_{sen} must contain enough data points to meet that requirement. The per-segment sensitivity of a FOS is affected by the spectral resolution which depends on the signal-to-noise ratio in the FOS system. In general, the higher the number of data points per segment, the higher the spectral resolution and thus sensitivity. The actual best-case per-segment sensitivity is estimated *in-situ* on the fiber experimentally by comparing the standard deviations of spectral shifts obtained from cross correlations of a series of Rayleigh scatter spectra with different segment lengths, all measured at the same temperature and strain [21, 24]. As an example, assuming that the temperature sensitivity is proportional to the number of data points in a segment, and that it is found to be 2 K per 50 points (per segment, given $\Delta x = pL/K$ = 0.5 cm), then the data points p' required to attain a per segment sensitivity δT [K per segment] is $p' = 2\text{x}50/\delta T$ (note that p' here is actually inversely proportional to δT, due to the fact that lower values of δT represent higher sensitivity). Therefore, the minimum segment size required to attain sufficient sensitivity is $\Delta x_{sen} = p'L/K = 100L/(K\delta T)$ [cm] = $1/\delta T$ [cm]. By requesting δT = 3.7 K per segment, one gets Δx_{sen} = 1/3.7 cm = 0.27 cm, which is smaller than the selected Δx (= 0.5 cm).

If the calculated Δx_{sen} is larger than the chosen Δx, then the resolutions Δx and Δt must be adjusted, and Δx_{sen} reevaluated with the new resolutions until $\Delta x_{sen} <= \Delta x$ is satisfied. For example, suppose that the lower bound of dT_{mpz}/dx = 3.6 K, then it requires that δT = 3.6 K/cm x 0.5 cm = 1.8 K per segment and so Δx_{sen} = 1/1.8 cm = 0.56 cm, which is greater than the chosen Δx (= 0.5 cm). Without changing Δt, one can increase Δx = 0.6 cm, which is now in the new shaded admissible zone bounded by Δx_{sen} = 0.56 cm. With the new Δx = 0.6 cm, the new δT = 2.16 K and the new Δx_{sen} = 0.46 cm, which is now smaller than the new Δx. Lastly, note that in practice the average lower bounds of dT_{mpz}/dx and dT_0/dt are used; if they vary over relatively wide ranges then one should consider setting the required temperature sensitivity higher than the sensitivities derived from the average bounds.

V. A Conceptual Quench Detection Algorithm Based on a DTS

A DTS provides a quench detection algorithm a complete temperature distribution along the length of conductor in the coil, so a new approach to quench detection algorithm development is required. Figure 9 demonstrates a scenario where the hot spot has propagated from one turn to

adjacent turns. The radial correlation in hot spots can be a powerful discriminator between quenches and false positives. However, the true power of the radial correlations depends on the radial propagation speed, which depends on the details of turn-to-turn insulation amongst other factors.

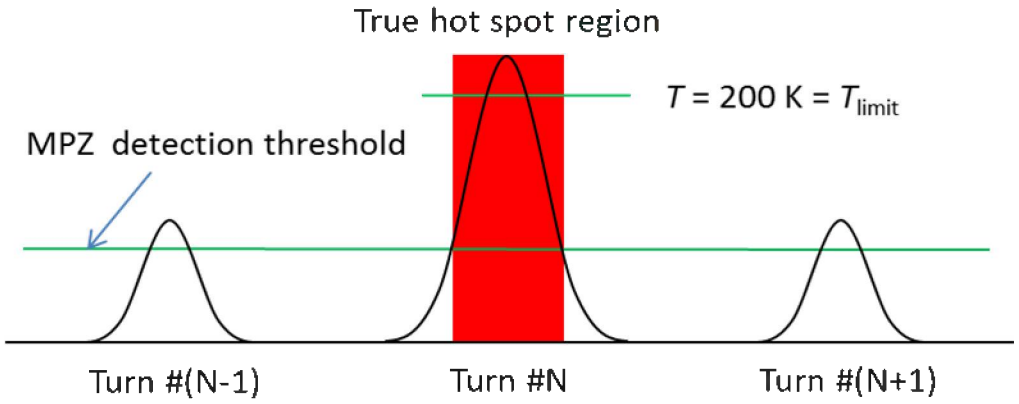

Figure 9. A distributed temperature profile showing heat propagation from the hot spot to adjacent turns.

Given a heat disturbance-independent MPZ, the following algorithm concept provides simple, quick and effective quench detection:

1. Scan for rising T, with appropriate spatial resolution Δx and temporal resolution Δt.
2. Search for a hot-spot, and if located, remember the hot-spot location. All following actions will be performed in a predefined neighborhood around the hot-spot location. The algorithm must have the capability to do this for numerous hotspots simultaneously.
3. Loop
   - I. Scan for normal zone size (NPZ) as $T >= T_{mpz}$, with resolutions Δx and Δt.
   - II. If NPZ >= MPZ + δX then flag QUENCHED (δX gives a safe margin and also takes into account the error margin in the T measurement).
     - a) Activate quench protection.
     - b) Stop.
   - III. If NPZ < MPZ and shrinks then flag RECOVERED.

Note that if NPZ < MPZ, the NPZ may shrink, and once it begins to shrink it will not expand again without additional heat input (i.e., another disturbance). If an NPZ is created by a transient heat disturbance and becomes NPZ > MPZ, it may shrink initially when the disturbance ends, but it will remain greater than MPZ and the coil will quench.

VI. Discussion

VI.A. Non Steady State Operation Issues.

Strain and temperature changes are not distinguishable within the Rayleigh scatter spectra, and what is measured is usually a combined effect. The relationship between a frequency shift $\Delta\nu$ obtained from a cross correlation and the temperature change ΔT and strain ε is:

$$-\frac{\Delta\nu}{\nu} = K_T \Delta T + K_\varepsilon \varepsilon \tag{3}$$

where K_T is the sum of the thermal expansion coefficient and the thermo-optic coefficient, and K_ε is the strain coefficient. From equation (3), it is clear that a spectral/frequency shift obtained from a cross correlation of a Rayleigh scatter spectrum (with a reference spectrum) cannot determine whether the local change in the inherent signature is due to a change in temperature or strain. Strains can be caused by quench-induced thermal stresses or by the Lorentz forces that occur in magnets during operation. This strain-temperature coupling problem is complicated by the fact that the strain distribution within a magnet is inherently non-uniform. FOS based quench detection is not concerned with the separation of strain and temperature contributions, but whether the combined behavior does not match the expected behavior.

For AC systems or ramping magnets one needs to construct a series of reference scans that correspond to the expected non-quench fiber state at a given current. This is challenging, as it requires the storing of a lot of data and the loading of a new reference for each scan. The reference scan update granularity, with respect to current (ramping systems) or phase (AC systems) intervals, must be included in coil specific optimizations. The data processing burden can be limited by pre-computing the expected temperature/strain shift from the known spectra. This reduces the problem to one of correcting N segments with N constants and using a single baseline spectrum. The corrections can be stored in simple look up tables that are very efficient to use and can be partitioned as a function of the current (or phase) to make the problem cache-able and thus not diminishing performance of the overall system too much.

To correct a ramping system one must have a way to predetermine or predict what the spectra for expected behavior will look like. This is a concern for the first ramp, after which one will have enough data to construct all of the required spectra. A possible method of *a priori* estimation of non-quench reference scans for the initial excitation of a coil is to use non-quench strain/temp data from a coil model to determine the offset and relative differences along the conductor (and thus fiber) for a given current/force.

- Ramp to current
    - Remove from the data any constant fiber offset and relative differences based on the coil model.
    - Scan N-times at that current to determine if there is any time dependent behavior.
    - Record actual fiber data to construct reference data for subsequent ramps.
    - Determine the level of agreement between the experimental data and the model
        - Predict the magnitude and relative differences of the next current step based on the coil model and current fiber data. Use this in a feed forward manner for each subsequent current step.
- Ramp to next current step and repeat the above steps.

VI.B. Selection of optimal resolutions

Within the shaded admissible zones in Figure 7 or 8, the selection of the optimal resolutions Δx and Δt are determined by the quality of the measured Rayleigh backscattering signal and the time budgets needed for strain-temperature decoupling (if necessary) and protection. Here the quality of a measured signal refers to the quality affected by the implementation of the measurement setup, independent of the background noise inherent in the FOS system. Background noise dictates the signal-to-noise ratio and only affects the lower bound of Δx (as Δx_{sen}). Large temperature or strain gradients due to implementation defects or imperfection in co-winding the optical fiber with the conductor are examples that affect the quality of a measured signal. A poor quality signal results in a noisy, spread-out cross correlation (spectral shift) peak. In this case, the quality of the cross correlation can only be improved with higher spatial sampling resolution

(smaller Δx), rather than with higher sensitivity. The key is that the condition $\Delta x_{sen} <= \Delta x$ must still hold. A general guide is to choose the smallest allowable Δx and Δt within the shaded admissible zone. The choice of the smallest allowable Δx may result in capturing unwanted details such as implementation defects. However, since these kind of details are rather static, they can be discriminated from real quench-induced changes via algorithm. The choice of the smallest allowable Δt is justified by the fact that it may take a Δt measurement iteration to successfully capture a MPZ if the current Δt iteration does not detect the MPZ. Therefore, the larger the Δt, the longer it takes to capture a MPZ, resulting in a tighter time budget for protection.

Using the same pancake coil example, suppose it takes $2\Delta t_{daq}$ to convert a single Rayleigh scatter scan into temperature, plus an additional 20 ms to decouple the strain if necessary. It also takes up to $2\Delta t$ to capture a MPZ soon after it is formed, and as short as 180 ms for a hot spot to rise from T_c = 89 K to 100 K (e.g., see $T_{60_0.5}$(>>MQE) in Figure 1). Here 100 K is used as the maximum temperature for a given protection circuit to activate the dumping process to dissipate enough stored energy before the hot-spot temperature reaches the safe limiting temperature of, for example, 200 K. In other words, the time budget to protect the magnet is 180 ms. Thus, $2(2\Delta t_{daq} + 20 \text{ ms}) <= 180$ ms, which gives $\Delta t_{daq} <= 35$ ms. From the $\Delta t_{daq} = f(\Delta x)$ graph in Figure 8, the smallest Δx that can be chosen is Δx = 0.7 cm, with Δt_{daq} = 35 ms. So the optimal resolutions when all of the timing and quality factors are taken into account become Δx = 0.7 cm and Δt = 2 x 35 ms + 20 ms = 90 ms, as marked by the X in Figure 8. Following the previously discussed sensitivity analysis, from dT_{mpz}/dx, the per-segment sensitivity δT = 7.4 K/cm x 0.7 cm = 5.18 K and from dT_0/dt, δT = 90 K/s x 90 ms = 8.1 K. Using the same equation to calculate Δx_{sen}, one gets Δx_{sen} = 1/5.18 [cm] = 0.19 cm, which is smaller than the required Δx = 0.7 cm, so no further adjustment in Δx (and Δt) is required.

VII. Conclusion

This paper addresses the issues critical to the successful implementation of reliable quench detection for a YBCO based magnet using Rayleigh scattering within optical fibers, which offers real-time distributed temperature sensing with excellent spatial resolution. The key challenge is to find the optimal spatial and temporal resolutions that allow reliable and efficient quench detection within the computational capability of a data acquisition and processing system. Here an experimentally validated, 3D multiscale YBCO coil model is used to analyze quench characteristics related to the identification of such resolutions. Simulation results show that MPZ, which is independent of the unpredictable heat disturbance, is the key quench parameter to enable the determination of the spatial and temporal resolutions.

Based on MPZ, a systematic method for finding the optimal spatial and temporal resolutions is derived. Challenges facing the implementation of Rayleigh scattering based fiber optic sensing, including the decoupling of strain effect from temperature measurement and the special consideration for a quench detection algorithm based on distributed temperature sensing are discussed.

Technology Benchmarking

Based on the previous section we see that processing time and data volume are the key challenges for a fiber optic Rayleigh scattering quench detection system. In this section in figures 10 through 14 we present the benchmarking studies of the relevant technologies. After

considering all of the information it was concluded that GPUs were the most appropriate choice for accelerating the signal processing. The issue of running them under real time operating systems can be addressed by development of a real-time compatible driver (this was not pursued in this project as it is a major multi-year project in itself. As will be seen later we hid the GPU system behind a real-time layer, this was a prudent approach given the constraints of the project. The decision to pursue a GPU based system over a multi-core CPU based system was motivated by a 10 ms timing target. The decision to pursue a GPU based system over an FPGA based system was motivated on the level of risk of successfully developing a FPGA based system that could handle a 512K-point FFT. While not impossible, it was clear that not enough was known about the performance one could expect when issues such as FPGA latency and I/O bandwidth were considered. A multi-core approach could be developed directly in the context of an RTOS. However, for quench detection we have a target time <10 ms, lower than that achievable with simple multi-core machines. Additionally, of the 12 cores, several are required to handle data I/O, control, trigger algorithms, and target-host communication etc. Therefore, the performance would be downgraded in the transition from benchmarking to a real system. Further details can be found in [32].

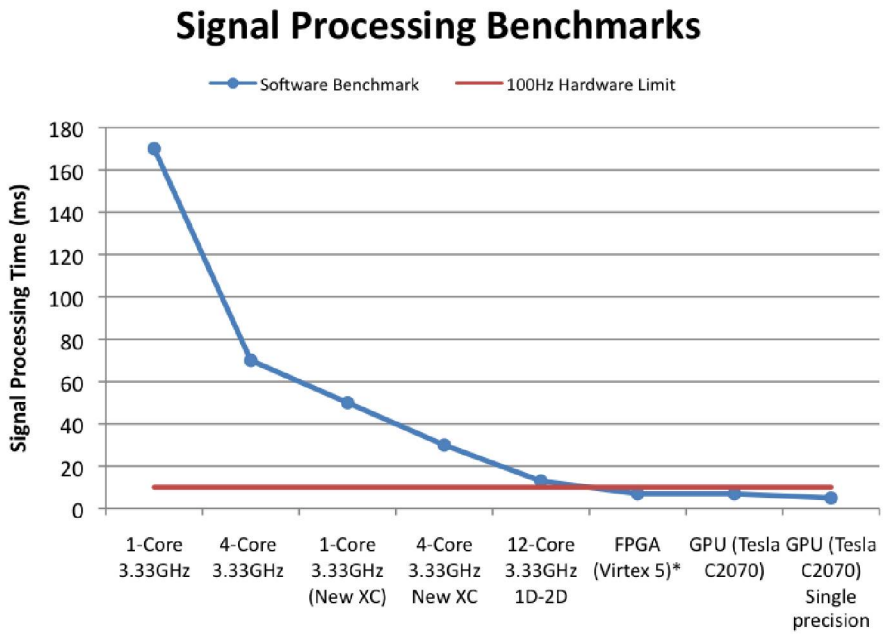

Figure 10. Summary of the signal processing benchmarking study. The signal processing time is the time taken to perform either 512K point FFT+500 1024-pt FFT's or 512K point FFT + 5120 100-pt FFT's. Both configurations were checked and found to be consistent (within statistical uncertainty). The FPGA (*) approach was discounted when it became clear that the risk was too high and the performance gain over a GPU did not look significant enough to justify it. From the plot it is clear that both multicore PCs and GPUs are promising technologies. GPUs were found to be faster for this particular application. Additionally, GPUs allow the PC's cores to be used more efficiently for I/O, control, and running decision algorithms.

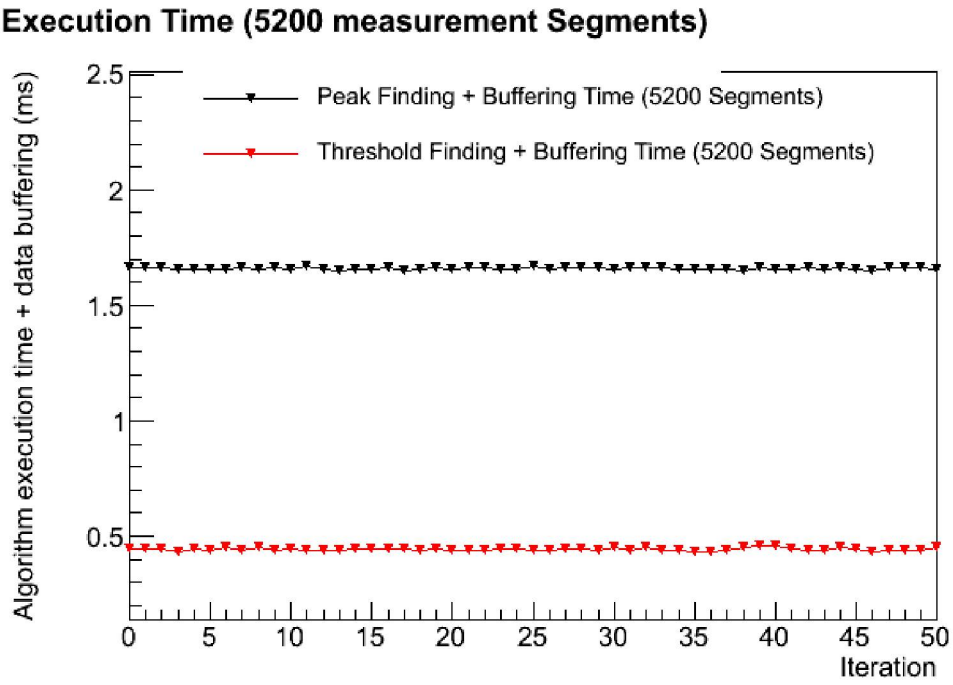

Figure 11. Comparison of the time taken to process 5120 segments and find a quench using peak detection or looking for data above threshold. Looking for segments above predefined thresholds is more appealing due to the speed and simplicity. Thresholding data will be the basis of the Phase II algorithm, however, the ability to look for peaks will be retained in the code. Threading the search algorithms across multiple cores can reduce the trigger decision time further.

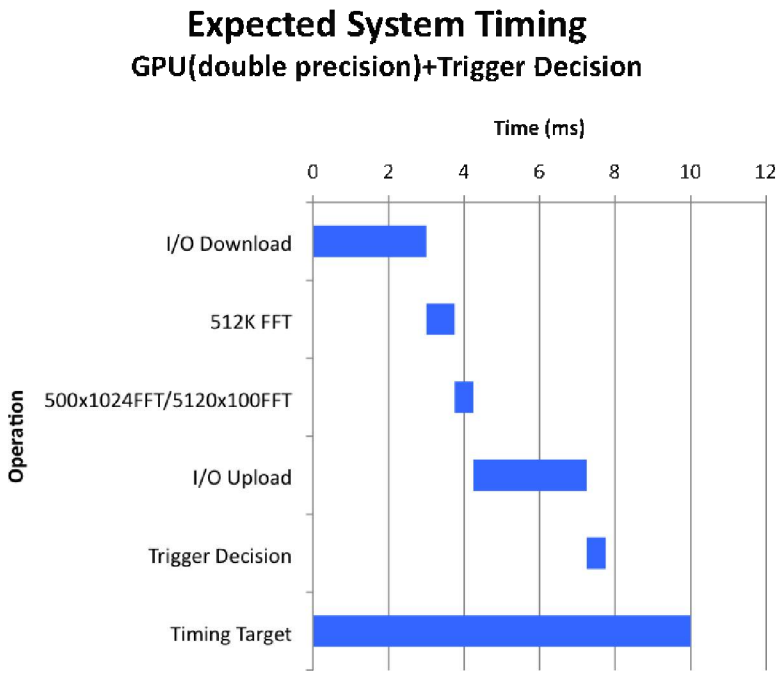

Figure 12. The timing structure of the GPU based signal processing (Tesla series c2070-double precision) plus the quench signal finding and decision timing. The total system time (based on benchmarks) is faster than the timing target set by the interrogator (10ms acquisition time). The 3rd entry reflects the fact that doing 500(1024-pt FFT's) segments took the same amount of time as doing 5210 (100-pt FFT's) . The trigger decision time corresponds to scanning 5120 segments. Threading the search algorithms across multiple cores can reduce the trigger decision time further.

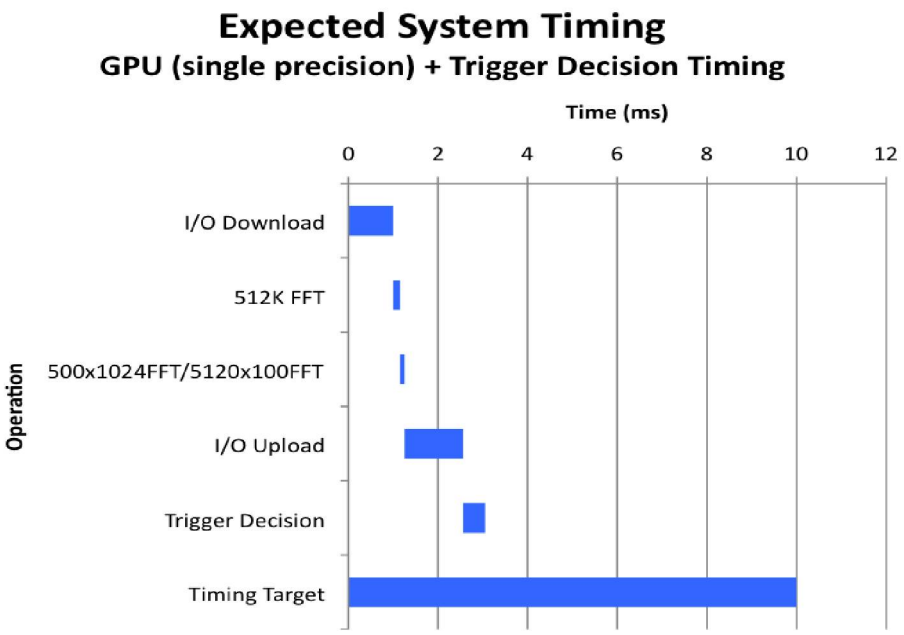

Figure 13. The timing structure of the GPU based signal processing (Tesla series c2070-single precision) plus the quench signal finding and decision timing. The total system time (based on benchmarks) is much faster than the timing target set by the interrogator (10 ms acquisition time). The 3rd entry reflects the fact that doing 500(1024-pt FFT's) segments took the same amount of time as doing 5210 (100-pt FFT's). The trigger decision time corresponds to scanning 5120 segments. Threading the search algorithms across multiple cores can reduce the trigger decision time further.

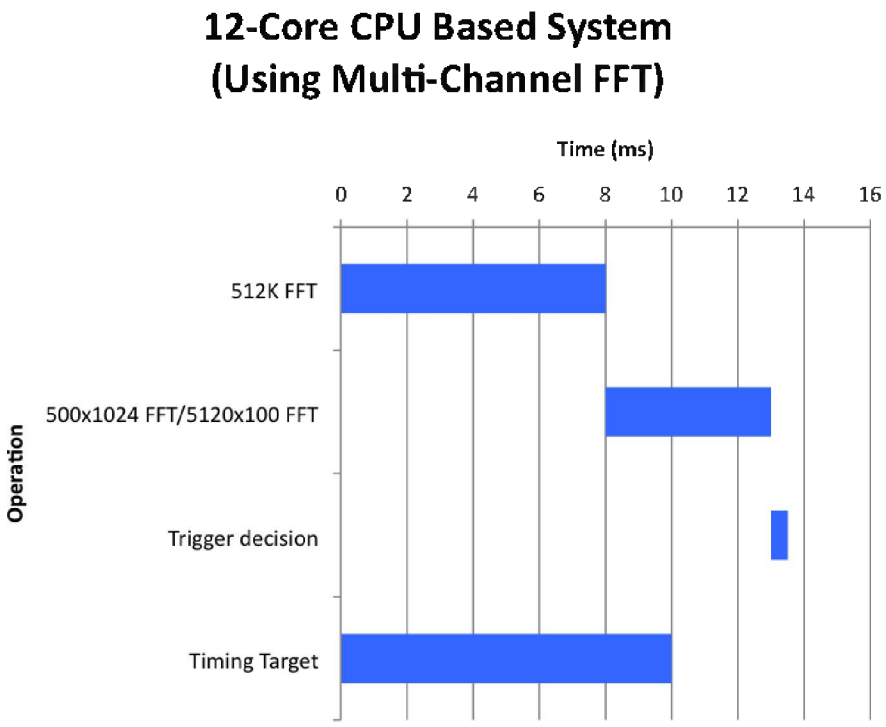

Figure 14. The timing structure of the 12-core based signal processing plus the quench signal finding and decision timing. The impressive performance for the 512K-point FFT comes from using the multichannel FFT approach. The 3rd entry reflects the fact that doing 500(1024-pt FFT's) segments took the same amount of time as doing 5210 (100-pt FFT's). The trigger decision time corresponds to scanning 5120 segments. Threading the search algorithms across multiple cores can reduce the trigger decision time further.

Quench Detection System Details

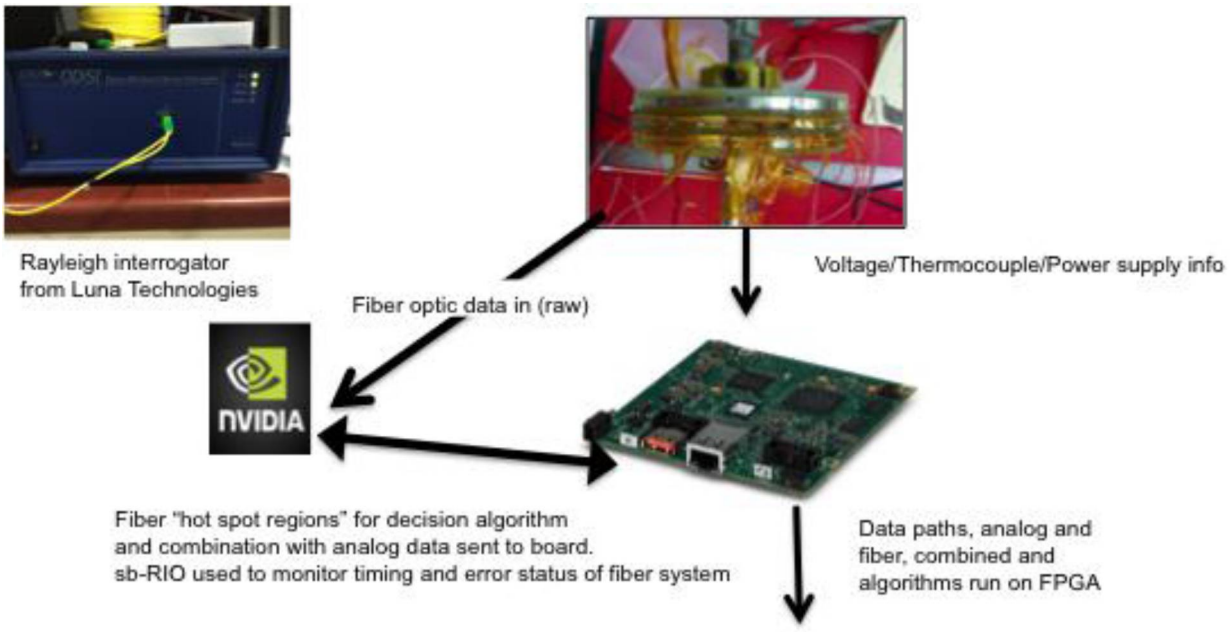

Figure 15. The final system was based on a Rayleigh Backscatter Reflectometer from Luna Technologies, the raw swept wavelength interferometer data was processed on an Nvidia GPU, the data is then sent to a multi-core PC where an algorithm checks the processed fiber data for a segment with maximum change, also the 10 neighboring segments to calculate normal zone evolution. Additional normal zones on unused segments (i.e. not included in previous normal zone) are also identified. This data is combined with analog voltage data on an FPGA. The calculated (from the fiber data) evolution of the normal zone is correlated spatially with voltage data. System can be seen diagrammatically in figure below. The FPGA board provides an easy way to interface with all other peripheral systems, and provides strict timing checks and controls.

System Testing and Coil Results

Experimental Details

Several superconducting YBCO coils have been fabricated and instrumented with optical fiber, voltage taps and thermocouples. In both coils the optical fiber was co-wound with the conductor, but the two coils differ in the relative position of optical fiber and conductor. In coil I, the optical fiber is atop the conductor and in coil II the fiber is along the conductor edge where it also serves as turn-to-turn insulation. Both coils are single layer helical coils wound on a G-10 coil former; these are seen in Figure 1. Voltage taps (VTs) have been soldered to the conductor using a 60/40 Sn/Pb solder with a 2-cm spacing. Thermocouples have been attached via the same solder, except for the on atop the heater section that was glued with GE Varnish. A heater, consisting of a Ni-Cr insulated wire, was shaped to cover the conductor surface between two VTs and also attached via GE Varnish. Lastly, after all instrumentation is attached, the coils were painted with GE varnish. Figure 2 illustrates the wiring schematics for both coils.

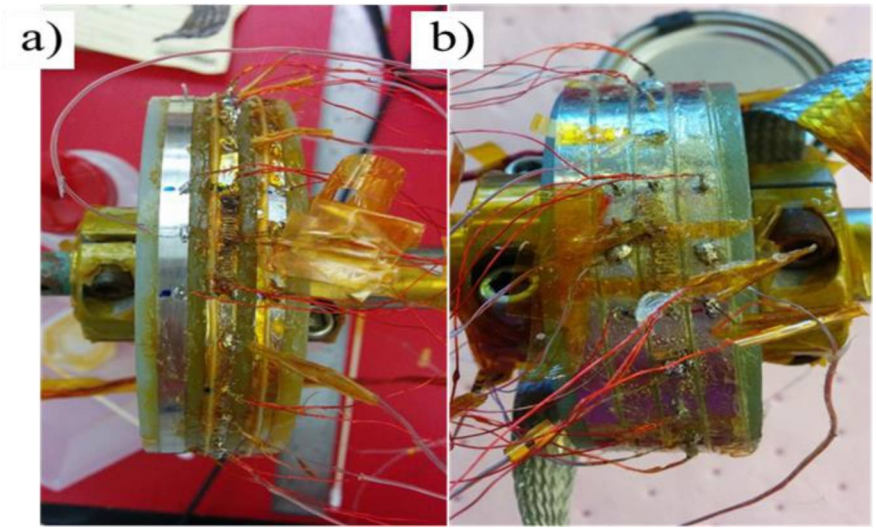

Figure 16. Two instrumented YBCO coils used in this study: a) coil I, with the optical fiber co-wound atop the conductor and b) coil II, with the optical fiber is co-wound between conductors as turn-to-turn insulation.

Each coil was mounted on a probe equipped with current leads and inserted into a cryostat filled with liquid nitrogen. The temperature, voltage and spectral shift were measured as a function of time at different locations along the coil. The RIOF were interrogated using a commercial optical distributed sensor interrogator (model ODiSI-B by from Luna Technologies Inc.), which measures the spectral shift as a function of time and position along the fiber. The optical fiber was connected to the ODiSI B and all the voltage taps and thermocouples were connected to Keithley® 2700 digital multi meters (DMMs). The ODiSI-B, DMMs and heater were controlled by software/firmware written within LabView® .

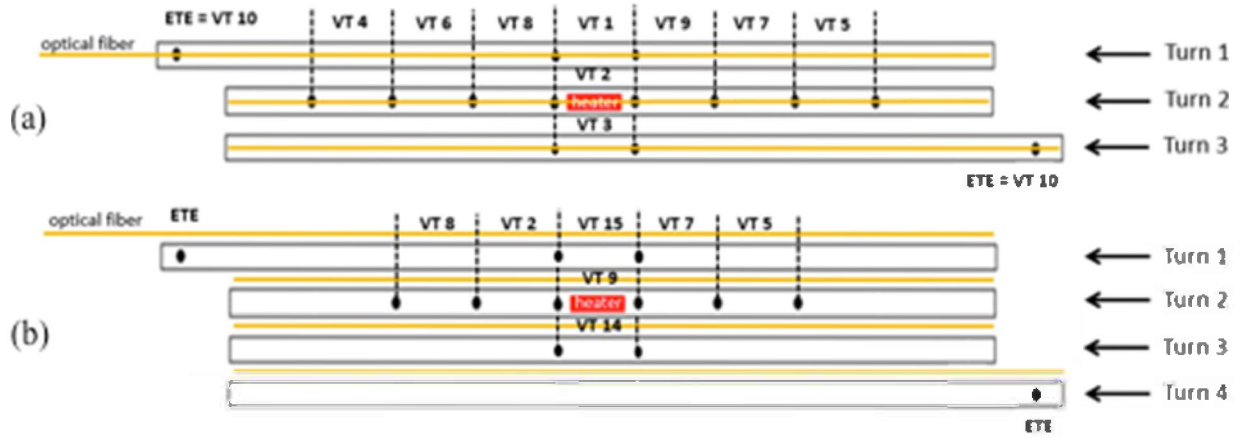

Figure 17. Schematic instrumentation diagrams for the two coils shown in Figure 16. In both coils the voltage tap spacing is 2 cm and a voltage tap is located between each voltage-tap pair.

The coil temperature is varied by either submersing the entire coil into the liquid nitrogen for 77 K experiments, or by lowering the coil close to but not within the liquid, such that the coil is nitrogen vapor cooled to a temperature near but above 77 K. Each quench experiment began with the coil at thermal equilibrium within the cryostat and in the superconducting state. A transport current was initiated in the coil and ramped to a set value (I_t). About 300 ms after the transport current reached I_t, the heater was powered by applying a constant voltage with a power supply for a certain duration. The spectral shift in the optical fiber as a function of position along the fiber and time was continuously interrogated by the ODiSI-B, as were the voltage and temperature.

The software controlling the ODiSI-B divides the fiber into 5 mm long segments, defining the spatial resolution for this experiment. Each interrogation cycle requires ~30 ms, after which the measurement is repeated. Thus the spectral shift is measured and compared to the reference scan as a function of space and time, with 5 mm spatial resolution and 30 ms time resolution. To decrease the data processing required to compute the spectral shift, during each measurement cycle, the LabView® software recorded the data coming from the four positions along the fiber that experienced the four highest spectral shifts, as well as the ten segments neighboring each of them. The remaining data were discarded. This reduces dramatically the measurement time, yet still enables the measurement of the normal zones size and evolution. We refer to these four positions, along with the 10 neighboring segments, as the hot-spot. It is worth noting that the position of the hot-spot along the fiber varies with time, as the locations experiencing the highest combination of temperature and strain evolves with time. This evolution is also captured by the DAQ system.

Results & Discussion

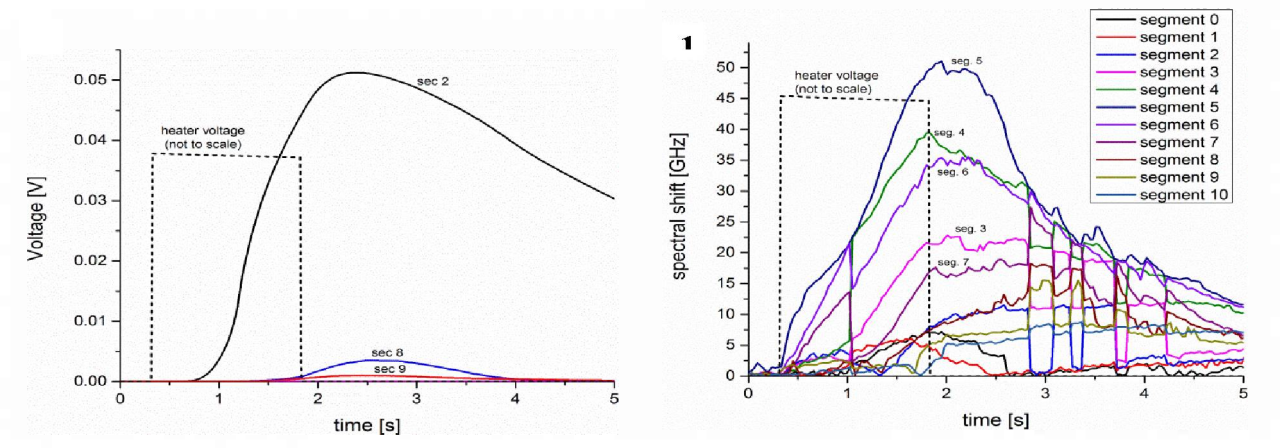

Figure 18. Results for an experimental run with Coil I (with fiber atop the tape) during which the coil did not quench: a) voltage versus time, b) spectral shift versus time. In (b), segments 0 to 10 refers to successive 5-mm long fiber segments, centered about the segment with the highest spectral shift (always segment 5), the hot-spot.

Figure 18 shows results from coil I with the fiber atop the conductor for an experimental run at 77 K and a transport current of 150 A, as compared to the self-field I_c of 135 A. Note that here I_c is defined as the lowest critical current obtained monitoring all the voltage sections as well as an end-to-end voltage tap. Note also that, because of the effectiveness of liquid nitrogen cooling, the

coil did not quench. Figure 18(a) shows the voltage versus time; a measureable voltage appears and increases about 400 ms after the initiation of the heat pulse, whereas Figure 18(b) shows a non-zero spectral shift immediately after the heat pulse begins.

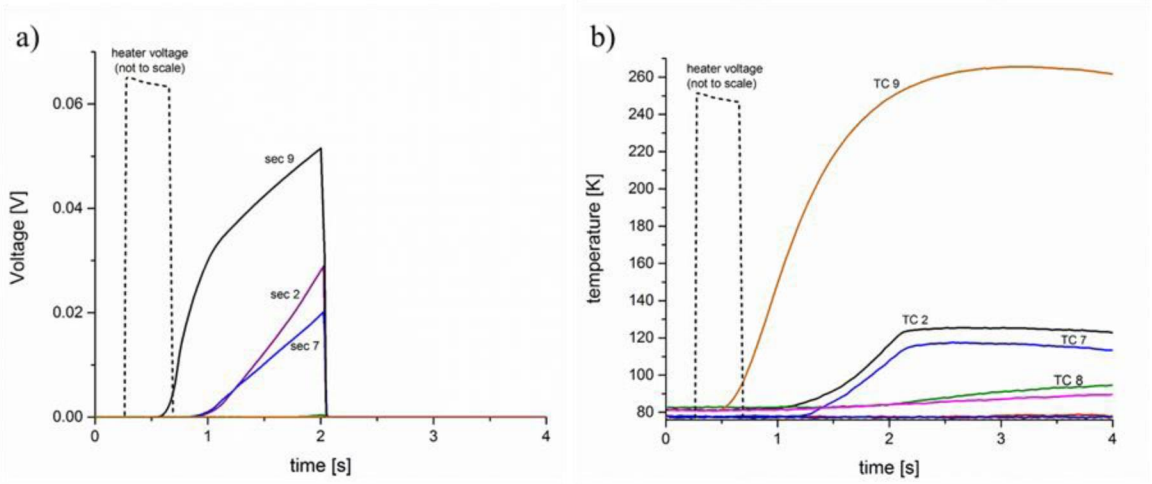

Figure 19. Results for an experimental run with Coil II (with fiber next to the conductor edge) during which the coil quenched: a) voltage versus time, b) temperature versus time, c) spectral shift at the hot-spot versus time, and d) time evolution of the hot-spot location.

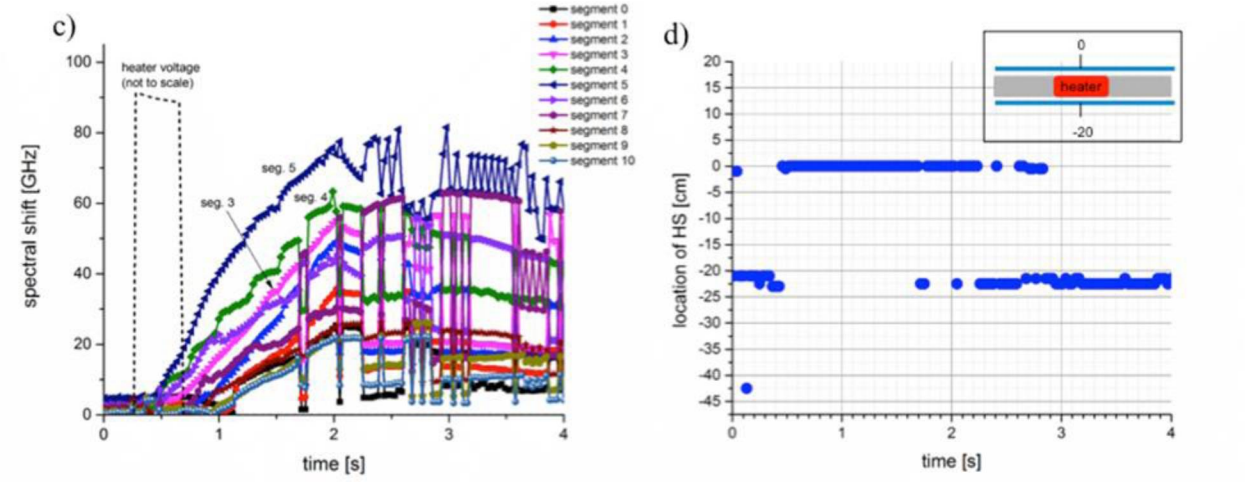

Figure 20. Results for an experimental run with Coil I during which the coil quenched: a) spectral shift at the hot-spot and voltage measured at section 2 (across the heater) as a function of time and b) hot-spot location as a function of time

The results of a quench in coil II are shown in Figure 19 and Figure 20. In this case, the coil just above the liquid level in the cryostat and cooled by nitrogen vapor. The highest temperature on the coil (furthest from the liquid) just before the experiment began was 87.2 K. The transport current in the coil was then increased linearly to 126 A, corresponding to 90% of I_c (self-field, 77 K). The heat pulse duration was 400 ms and was sufficient to cause a quench. The voltage limit is reached after 2 s, at which time the transport current returns to zero and both the temperature measured by the thermocouples (Figure 19a/b) and the spectral shift (Figure 20c/d) begin to decrease. Similar to the previous case, a detectable voltage (Figure 19a) is first observed 270 ms

after the heat pulse begins, whereas the spectral shift signal begins 60 ms earlier. The time delay for the thermocouples is similar to that of the spectral.

The spectral shifts at the 11 segments constituting and surrounding the *hot-spot* are plotted versus time in Figure 20c, where the hot-spot is defined as the location of the segment with the maximum spectral shift. The hot-spot is designated segment 5. The spatial information is represented by the time evolution of the location of the hot-spot, shown in Figure 20d. Note that in coil II the fiber runs along the conductor edges (see inset of Figure 20d, or Figure 16 or 17) and thus two fiber locations are symmetric about the conductor, here defined as 0 and -20 cm. Consistently, after the heat pulse, the location of the hot-spot hops between these two positions, indicating that the hot-spot is in the middle of the conductor, and also illustrating the sensitivity of Rayleigh scattering interrogation. Thus, the coil II geometry, with the optical fiber co-wound along the conductor edges, has the advantage of having a "double check" for finding the hot-spot location, as the fiber on each side of the hot-spot shows a spectral shift. Figure 21 shows the results from a run with coil I with analogous experimental procedure and a transport current of 93%I_c. In particular, Figure 21a shows the heat pulse, the voltage measured across the heater and the hot-spot spectral shift, and the hot-spot location as a function of time is plotted in Figure 21b. Due to the coil geometry, with the fiber atop the conductor, coil I only presents one location where the fiber is closest to the heater, defined here as segment zero. After the heat pulse, the hot-spot location is constant for 2 s and then moves by as much as 6 cm during the next 3 s. The spectral shift magnitude at the hot-spot confirms that when the hot-spot location begins to move, the thermal perturbation is nearly zero. This indicates that the Rayleigh interrogation approach captures the fine-scale details of both a quench and during recovery. In fact, without any perturbation, the "hot-spot" location, i.e., the location indicating some changes in spectral shift, changes with time spanning the entire fiber.

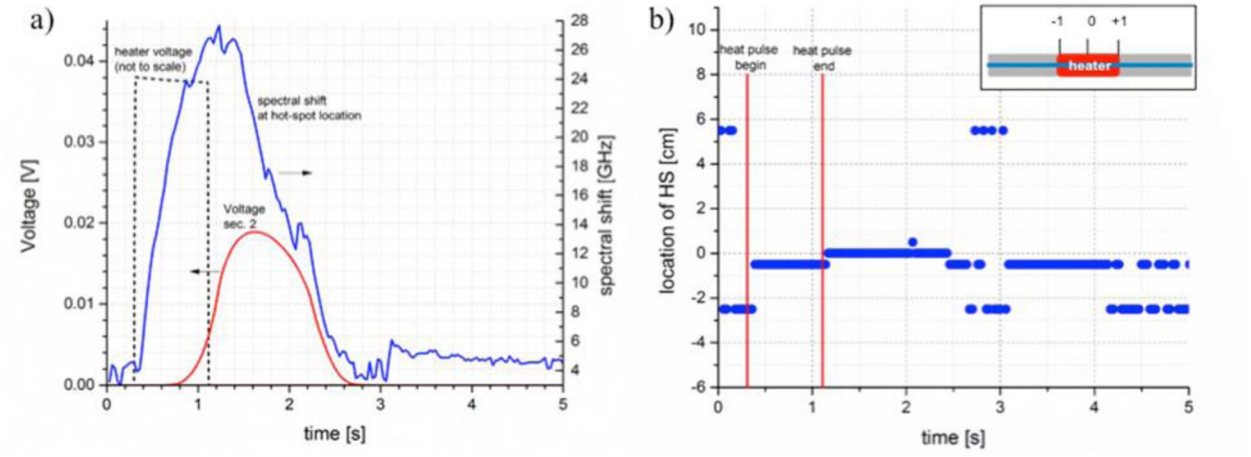

Figure 21. Results for an experimental run with Coil II during which the coil quenched, showing only the first second of the experiment, illustrating the relative time delays for voltage, thermocouple and fiber sensors.

Figure 22 demonstrates again that, after the perturbation, the increase in spectral shift precedes that of a non-zero voltage. The reason for this difference is that a non-zero voltage does not occur until the temperature at some location between the voltage taps exceeds the current sharing temperature, T_{cs}, whereas a spectral shift results from any change in temperature or strain.

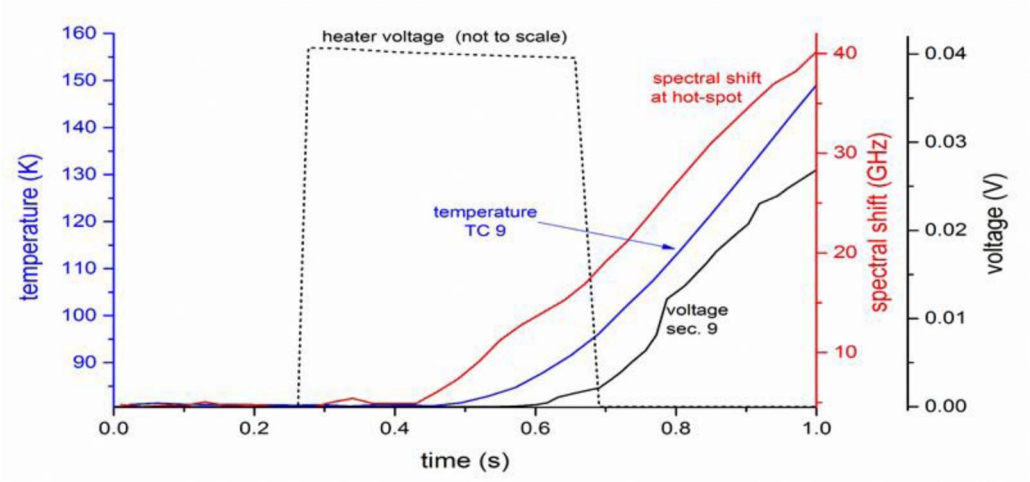

Figure 22. Time delays for measureable voltage and spectral shift signals (above background) versus I/I_c for a series of experiments on coil I.

Comparison between the voltage, temperature and spectral shift profiles are plotted in Figure 21 for a quench in coil II. The time difference between the onset of a measureable spectral shift and voltage is much longer than that between spectral shift and temperature, though even in the latter case there is a clear difference. Note again that as the voltage drops to zero when the transport current is zeroed, but the spectral shift and the temperature continue to monitor the transient. Thus, the distributed sensing of the optical fiber will clearly show when the coil has returned to thermal equilibrium after a protected quench.

The time delays between the onset of the heater to the onset of measureable voltage and spectral shift signals above any background noise from a series of quench runs on coil I, characterizing the responsiveness of the detection systems to a thermal perturbation, are plotted in Figure 22. The time delays are plotted against versus I/I_c, but note that other experimental conditions, such as the heater voltage and pulse duration and background temperature, vary somewhat from one test to another. Thus, for I/I_c of 48% and 74%, voltage delays are not plotted because they are infinite; i.e., the temperature did not rise above T_{cs}, whereas the spectral shift showed a signal after ~90 ms. As expected, when I/I_c is sufficiently large to induce a temperature rise above current sharing, the voltage delay becomes finite and decreases further as the current increases further. The spectral shift delay is always finite and does not show broad variance. In the experiments here, the strong nitrogen cooling environment and the small-size of the coils results in coils that are difficult to quench. Thus, to observe differences in quench detection, large values of I/I_c were required. Yet the advantages of Rayleigh-backscattering interrogated optical fibers are clear. Furthermore, as I/I_c decreases to values that are more realistic for superconducting magnet applications in service, the difference in detection speed increases rapidly. Lastly, in general the spatial resolution available via voltage taps decreases as the size of the coil increases, whereas the spatial resolution of RIOF is independent of coil size and tunable.

Bibliography and References

[1] J. Schwartz, T. Effio, X. Liu, Q. V. Le, A. L. Mbaruku, H. J. Schneider-Muntau, *et al.*, "High field superconducting solenoids via high temperature superconductors," *IEEE Transactions on Applied Superconductivity,* vol. 18, pp. 70-81, Jun 2008.

[2] A. Godeke, D. Cheng, D. R. Dietderich, C. D. English, H. Felice, C. R. Hannaford, *et al.*, "Development of wind-and-react Bi-2212 accelerator magnet technology," *IEEE Transactions on Applied Superconductivity,* vol. 18, pp. 516-519, Jun 2008.

[3] W. D. Markiewicz, J. R. Miller, J. Schwartz, U. P. Trociewitz, and H. W. Weijers, "Perspective on a superconducting 30 T/1.3 GHz NMR spectrometer magnet," *IEEE Transactions on Applied Superconductivity,* vol. 16, pp. 1523-1526, Jun 2006.

[4] H. Miao, K. R. Marken, M. Meinesz, B. Czabaj, S. Hong, A. Twin, *et al.*, "High field insert coils from Bi-2212/Ag round wires," *IEEE Transactions on Applied Superconductivity,* vol. 17, pp. 2262-2265, Jun 2007.

[5] G. Snitchler and J. M. Seuntjens, *High temperature superconductor composites for accelerator magnets* vol. 13. Singapore: World Scientific Publ Co Pte Ltd, 1998.

[6] U. P. Trociewitz, M. Dalban-Canassy, M. Hannion, D. K. Hilton, J. Jaroszynski, P. Noyes, *et al.*, "35.4 T field generated using a layer-wound superconducting coil made of (RE)$Ba_2Cu_3O_{7-x}$ (RE = rare earth) coated conductor," *Applied Physics Letters,* vol. 99, p. 3, Nov 2011.

[7] H. W. Weijers, B. ten Haken, H. H. J. ten Kate, and J. Schwartz, "Critical currents in Bi-Sr-Ca-Cu-O superconductors up to 33 T at 4.2 K," *IEEE Transactions on Applied Superconductivity,* vol. 11, pp. 3956-3959, Mar 2001.

[8] H. W. Weijers, U. P. Trociewitz, K. Marken, M. Meinesz, H. Miao, and J. Schwartz, "The generation of 25.05 T using a 5.11 T $Bi_2Sr_2CaCu_2O_x$ superconducting insert magnet," *Superconductor Science and Technology,* vol. 17, pp. 636-644, 2004.

[9] J. Schwartz, F. Hunte, W. Chan, X. Gou, X. Liu, M. Phillips, *et al.*, "Status of high temperature superconductor based magnets and the conductors they depend upon," *arXiv preprint arXiv:1108.1634,* 2011.

[10] C. Senatore, M. Alessandrini, A. Lucarelli, R. Tediosi, D. Uglietti, and Y. Iwasa, "Progresses and challenges in the development of high-field solenoidal magnets based on RE123 coated conductors," *Superconductor Science & Technology,* vol. 27, Oct 2014.

[11] P. J. Masson, M. Breschi, P. Tixador, and C. A. Luongo, "Design of HTS axial flux motor for aircraft propulsion," *IEEE Transactions on Applied Superconductivity,* vol. 17, pp. 1533-1536, Jun 2007.

[12] A. B. Abrahamsen, N. Mijatovic, E. Seiler, T. Zirngibl, C. Traeholt, P. B. Norgard, *et al.*, "Superconducting wind turbine generators," *Superconductor Science & Technology,* vol. 23, p. 8, Mar 2010.

[13] D. U. Gubser, "Superconducting motors and generators for naval applications," *Physica C-Superconductivity and Its Applications,* vol. 392, pp. 1192-1195, Oct 2003.

[14] G. Snitchler, B. Gamble, and S. S. Kalsi, "The performance of a 5 MW high temperature superconductor ship propulsion motor," *IEEE Transactions on Applied Superconductivity,* vol. 15, pp. 2206-2209, Jun 2005.

[15] J. S. Wang, S. Y. Wang, C. Y. Deng, Y. W. Zeng, H. H. Song, and H. Y. Huang, "A superhigh speed HTS Maglev vehicle," *International Journal of Modern Physics B,* vol. 19, pp. 399-401, Jan 30 2005.

[16] J. S. Wang, S. Y. Wang, Y. W. Zeng, C. Y. Deng, Z. Y. Ren, X. R. Wang, *et al.*, "The present status of the high temperature superconducting Maglev vehicle in China," *Superconductor Science & Technology,* vol. 18, pp. S215-S218, Feb 2005.

[17] S. Y. Wang, J. Zheng, H. H. Song, X. Z. Wang, and J. S. Wang, "Experiment and numerical calculation of high temperature superconducting Maglev," *IEEE Transactions on Applied Superconductivity,* vol. 15, pp. 2277-2280, Jun 2005.

[18] V. Selvamanickam, C. Yimin, X. Xuming, Y. Y. Xie, M. Martchevski, A. Rar, *et al.*, "High Performance 2G Wires: From R&D to Pilot-Scale Manufacturing," *Applied Superconductivity, IEEE Transactions on,* vol. 19, pp. 3225-3230, 2009.

[19] V. Selvamanickam, Y. Chen, X. Xiong, Y. Y. Xie, J. L. Reeves, X. Zhang, *et al.*, "Recent Progress in Second-Generation HTS Conductor Scale-Up at SuperPower," *Applied Superconductivity, IEEE Transactions on,* vol. 17, pp. 3231-3234, 2007.

[20] D. W. Hazelton, V. Selvamanickam, J. M. Duval, D. C. Larbalestier, W. D. Markiewicz, H. W. Weijers, *et al.*, "Recent Developments in 2G HTS Coil Technology," *Applied Superconductivity, IEEE Transactions on,* vol. 19, pp. 2218-2222, 2009.

[21] U. Schoop, M. Rupich, C. Thieme, D. Verebelyi, W. Zhang, X. Li, *et al.*, "Second generation HTS wire based on RABiTS substrates and MOD YBCO," *Applied Superconductivity, IEEE Transactions on,* vol. 15, pp. 2611-2616, 2005.

[22] M. W. Rupich, U. Schoop, D. T. Verebelyi, C. L. H. Thieme, D. Buczek, X. Li, *et al.*, "The Development of Second Generation HTS Wire at American Superconductor," *Applied Superconductivity, IEEE Transactions on,* vol. 17, pp. 3379-3382, 2007.

[23] L. Xiaoping, M. W. Rupich, C. L. H. Thieme, M. Teplitsky, S. Sathyamurthy, E. Thompson, *et al.*, "The Development of Second Generation HTS Wire at American Superconductor," *Applied Superconductivity, IEEE Transactions on,* vol. 19, pp. 3231-3235, 2009.

[24] D. C. Larbalestier, J. Jiang, U. P. Trociewitz, F. Kametani, C. Scheuerlein, M. Dalban-Canassy, *et al.*, "Isotropic round-wire multifilament cuprate superconductor for generation of magnetic fields above 30 T," *Nature Materials,* vol. 13, pp. 375-381, 04//print 2014.

[25] A. Ishiyama, M. Yanai, T. Morisaki, H. Ueda, Y. Shiohara, T. Izumi, *et al.*, "Normal transition and propagation characteristics of YBCO tape," *IEEE Transactions on Applied Superconductivity,* vol. 15, pp. 1659-1662, Jun 2005.

[26] S. Ishmael, H. Luo, M. White, F. Hunte, X. T. Liu, N. Mandzy, *et al.*, "Enhanced Quench Propagation in $Bi_2Sr_2CaCu_2O_x$ and $YBa_2Cu_3O_{7-x}$ Coils via a Nanoscale Doped-Titania-Based Thermally Conducting Electrical Insulator," *IEEE Transactions on Applied Superconductivity,* vol. 23, Oct 2013.

[27] H. Song, K. Gagnon, and J. Schwartz, "Quench behavior of conduction-cooled $YBa_2Cu_3O_{7\text{-delta}}$ coated conductor pancake coils stabilized with brass or copper," *Superconductor Science & Technology,* vol. 23, Jun 2010.

[28] H. Song and J. Schwartz, "Stability and Quench Behavior of $YBa_2Cu_3O_{7-x}$ Coated Conductor at 4.2 K, Self-Field," *IEEE Transactions on Applied Superconductivity,* vol. 19, pp. 3735-3743, Oct 2009.

[29] F. Trillaud, A. Caruso, J. Barrow, B. Trociewitz, U. P. Trociewitz, H. W. Weijers, *et al.*, "Normal zone generation and propagation in $YBa_2Cu_3O_{7\text{-delta}}$ coated conductors initialized by localized, pulsed disturbances," in *Advances in Cryogenic Engineering, Vols 50a and B.* vol. 711, U. Balachandran, Ed., ed, 2004, pp. 852-859.

[30] F. Trillaud, H. Palanki, U. P. Trociewitz, S. H. Thompson, H. W. Weijers, and J. Schwartz, "Normal zone propagation experiments on HTS composite conductors," *Cryogenics,* vol. 43, pp. 271-279, 3// 2003.

[31] X. Wang, U. P. Trociewitz, and J. Schwartz, "Near-adiabatic quench experiments on short $YBa_2Cu_3O_{7-delta}$ coated conductors," *Journal of Applied Physics,* vol. 101, Mar 1 2007.

[32] X. Wang, U. P. Trociewitz, and J. Schwartz, "Self-field quench behaviour of $YBa_2Cu_3O_{7-delta}$ coated conductors with different stabilizers," *Superconductor Science & Technology,* vol. 22, p. 13, Aug 2009.

[33] X. R. Wang, A. R. Caruso, M. Breschi, G. M. Zhang, U. P. Trociewitz, H. W. Weijers, *et al.*, "Normal zone initiation and propagation in Y-Ba-Cu-O coated conductors with Cu stabilizer," *IEEE Transactions on Applied Superconductivity,* vol. 15, pp. 2586-2589, Jun 2005.

[34] T. Shen, L. Ye, D. Turrioni, and P. Li, "High-field quench behavior and dependence of hot spot temperature on quench detection voltage threshold in a Bi2Sr2CaCu2Ox coil," *Superconductor Science and Technology,* vol. 28, p. 075014, 2015.

[35] L. Ye, D. Cruciani, M. Xu, S. Mine, K. Amm, and J. Schwartz, "Magnetic field dependent stability and quench behavior and degradation limits in conduction-cooled MgB2 wires and coils," *Superconductor Science and Technology,* vol. 28, p. 035015, 2015.

[36] L. Ye, D. Cruciani, T. Effio, F. Hunte, and J. Schwartz, "On the Causes of Degradation in Round Wires and Coils by Quenching at 4.2 K," *Applied Superconductivity, IEEE Transactions on,* vol. 23, pp. 6400811-6400811, 2013.

[37] L. Ye, F. Hunte, and J. Schwartz, "Effects of high magnetic field on the quench behavior of Bi2Sr2CaCu2Ox coils at 4.2 K," *Superconductor Science and Technology,* vol. 26, p. 055006, 2013.

[38] L. Ye, P. Li, T. Shen, and J. Schwartz, "Quench degradation limits in multifilamentary Ag/Bi2Sr2CaCu2Ox conductors and evidence for a strain-driven degradation mechanism," *Superconductor Science & Technology*.

[39] X. Wang, U. P. Trociewitz, and J. Schwartz, "Critical current degradation of short YBa2Cu3O7-delta coated conductor due to an unprotected quench," *Superconductor Science & Technology,* vol. 24, Mar 2011.

[40] K. Peters, "Fiber Bragg grating sensors," *Encyclopedia of Structural Health Monitoring,* 2008.

[41] L. Cheng, R. Nieuwland, P. Toet, and K. Agovic, "Fiber Bragg grating sensors," in *Proceedings 2010 Annual Symposium of the IEEE Photonics Society Benelux Chapter, Delft, The Netherlands, November 2010, 149-152*, 2010.

[42] F. Hunte, H. Song, J. Schwartz, R. Johnson, and M. Turenne, "Fiber Bragg optical sensors for YBCO applications," in *Particle Accelerator Conference, Vancouver, Canada*, 2009.

[43] M. Turenne, R. Johnson, F. Hunte, and J. Schwartz, "Multi-purpose fiber optic sensors for high temperature superconductor magnets," in *Particle Accelerator Conference, Vancouver, Canada*, 2009.

[44] M. Turenne, R. Johnson, F. Hunte, J. Schwartz, and H. Song, "Multi-purpose fiber optic sensors for high temperature superconducting magnets," in *Fusion Engineering, 2009. SOFE 2009. 23rd IEEE/NPSS Symposium on*, 2009, pp. 1-4.

[45] S. Mahar, J. Geng, J. Schultz, J. Minervini, S. Jiang, P. Titus, *et al.*, "Real-time simultaneous temperature and strain measurements at cryogenic temperatures in an optical fiber," 2008, pp. 70870I-70870I-12.

[46] S. B. Mahar, "Spontaneous Brillouin Scattering Quench Diagnostics for Large Superconducting Magnets," Ph.D. dissertation, Massachusetts Institute of Technology, Department of Nuclear Science and Engineering, 2008.

[47] M. Froggatt and J. Moore, "High-spatial-resolution distributed strain measurement in optical fiber with Rayleigh scatter," *Applied Optics,* vol. 37, pp. 1735-1740, 1998/04/01 1998.

[48] D. K. Gifford, S. T. Kreger, A. K. Sang, M. E. Froggatt, R. G. Duncan, M. S. Wolfe, *et al.*, "Swept-wavelength interferometric interrogation of fiber Rayleigh scatter for distributed sensing applications," in *Optics East 2007*, 2007, pp. 67700F-67700F-9.

[49] D. K. Gifford, B. J. Soller, M. S. Wolfe, and M. E. Froggatt, "Distributed fiber-optic temperature sensing using Rayleigh backscatter," in *ECOC Proceedings*, 2005, pp. 511-512.

[50] W. K. Chan, G. Flanagan, and J. Schwartz, "Spatial and temporal resolution requirements for quench detection in (RE)$Ba_2Cu_3O_x$ magnets using Rayleigh-scattering-based fiber optic distributed sensing," *Superconductor Science and Technology,* vol. 26, p. 105015, 2013.

[51] G. Flanagan, R. Johnson, L. Wenzel, D. Schmidt, Q. Ruan, C. Wimmer, *et al.*, "Evaluation and implementation of high performance real-time signal processing for Rayleigh scattering based quench detection for high field superconducting magnets," *Proceedings of the International Particle Accelerator Conference* 2012.